

Diplomarbeit

Long distance transport of ultracold atoms using a 1D optical lattice

zur Erlangung des akademischen Grades
eines Magisters der Naturwissenschaften
vorgelegt von

Stefan Schmid

Institut für Experimentalphysik
an der Fakultät für Informatik, Mathematik und Physik
der Leopold-Franzens-Universität Innsbruck

Juli 2006

Danke!

Der harte aber durchwegs schöne Weg durch das Physikstudium und insbesondere die Anfertigung dieser Diplomarbeit als krönender Abschluss sind erst durch die Mithilfe einiger anderer Personen möglich geworden. Darum möchte ich hier die Gelegenheit nützen, diesem so wichtigen Umfeld meine Wertschätzung zeigen.

Als erstes möchte ich mich bei meinem Betreuer Johannes Hecker Denschlag bedanken. Sein motivierender Lob für die Erfolge, seine aufmunternden Worte in den Zeiten der Stagnation, seine konstruktive Kritik an den Fehlern: all das hat wesentlich zu meinen Erfolgen während der Diplomarbeit beigetragen.

Weiters will ich Rudi Grimm danken für das Aufnehmen in seine zweifelsohne herausragende Forschungsgruppe.

Ein besonderer Dank gilt meinen Laborkollegen Gregor, Klaus, Florian, Matthias und Sascha, die den Laboralltag für mich so unterhaltsam und angenehm gemacht haben. Vor allem die beiden Senioren Gregor und Klaus haben unzählig viel Zeit investiert, mir die Geheimnisse und Tricks unseres Experiments näher zu bringen. Jede einzelne Minute war wichtig und hat mir geholfen, die Dinge besser zu verstehen.

Natürlich gilt ähnlicher Dank auch dem Rest der Arbeitsgruppe für die so fruchtbare Zusammenarbeit.

Äusserst dankbar bin ich weiters noch Christoph Nägerl: Einerseits dafür, dass er bereits nach meinem ersten Studienjahr in mir die Begeisterung für die experimentelle Physik geweckt hat. Und aber vor allem dafür, dass er mir das Tor zu diesem fantastischen Jahr jenseits des Ozeans geöffnet hat.

Generell für den Beistand während des gesamten Studiums will ich meinen engsten Freunden danken. Nur durch deren offene Ohren für die vielen Probleme (rund um die Physik und auch abseits davon) sind diese vergangenen sechs Jahre so schön und interessant geworden.

Und natürlich danke ich Helga, meiner Mama.

Contents

1. Introduction	7
2. The optical lattice	9
2.1. The dipole potential	9
2.2. Laser beams	10
2.2.1. Gaussian beams	11
2.2.2. Bessel beams	12
2.2.3. Generation of Bessel Beams	13
2.3. Standing wave potentials	17
2.3.1. Gaussian beam lattice	17
2.3.2. Bessel-Gauss lattice	19
3. Atoms in moving lattices	21
3.1. Moving lattices - Classical approach	21
3.2. Moving lattices - Quantum optics approach	22
3.2.1. Transfer between momentum states	22
3.2.2. Adiabatic rapid passage	23
3.2.3. Mean velocity	27
3.3. Moving lattices - Solid state physics approach	29
3.3.1. Band structure	29
3.3.2. Accelerated lattice - Bloch oscillations	31
3.3.3. Atomic interactions and instabilities	33
4. Experiments with moving lattices	35
4.1. Experimental setup	35
4.1.1. Making a Bose-Einstein Condensate	35
4.1.2. Loading the standing wave trap	36
4.1.3. Setup for acceleration - creating a phase stable moving standing wave	39
4.2. Transport experiments	40
4.2.1. Basic Transport Kinematics	40
4.2.2. Transport of ultracold atoms using a Gaussian beam lattice	41
4.2.3. Transport of ultracold atoms using a Bessel-Gauss lattice	42
4.2.4. Transport of a BEC over macroscopic distances	44
4.2.5. Prominent features of the transport	47

4.3. Atom catapult	51
5. Conclusion & Outlook	53
A. Digital radio-frequency synthesizers	55
B. Phase Stabilization of Diode Lasers	59
B.1. Introduction	59
B.2. Feedback circuitry	59
B.3. Phase locked loops	60
B.4. Phase locked diode lasers	62
B.4.1. Diode lasers	62
B.4.2. Lockbox	67
B.4.3. Experimental setup	67
B.5. Results	69
B.5.1. The spectrum	69
B.5.2. Phase error	70

1. Introduction

The ever expanding field of ultracold atomic gases has recently entered several branches of physics for both fundamental physics experiments and but also applications. These include condensed matter physics, metrology, statistical physics, quantum information, molecular physics and many others. It is the unsurpassed control over the atomic degrees of freedom that is responsible for the success of the field. In order to extend these possibilities further and to expose ultracold atomic gases to new kinds of environments, transport of ultracold atoms over macroscopic distances is a key technology.

Within the framework of this diploma thesis I devised and tested a novel method to transport ultracold atoms over tens of centimeters with the help of an optical lattice.

Already before my work, transport of cold atoms has been of central interest for various groups who explored different kinds of approaches using magnetic and optical fields. A couple of years ago, several groups have reported using magnetic fields to move laser cooled atoms over macroscopic distances of tens of centimeters [Gre01, Lew02] or over smaller distances on an atom chip (for a review see [Fol02]). In the group of Wolfgang Ketterle a so-called optical tweezer has been realized [Gus02]. In this experiment a BEC is loaded into an optical dipole trap, which can be moved by mechanically relocating the focussing lens using a large translation stage. With this method they managed to transport the condensate over 40 cm within several seconds. A moving optical lattice offers another interesting possibility to transport ultracold atoms. In a simple picture, atoms are loaded into individual lattice sites and then are dragged along as the lattice is moved. Such a transport has been realized for example in the group of D. Meschede in Bonn where single, laser cooled atoms in a deep optical lattice were moved over short distances of a several millimeters [Kuh01]. Even beyond the field of ultracold atoms, applications of optical lattices for transport are of interest, where e.g. sub-micron sized polystyrene spheres immersed in heavy water were relocated [Ciz05].

In the framework of this thesis we experimentally investigate transporting BECs and ultracold thermal samples with an optical lattice over macroscopic distances of tens of centimeters. Our method features the combination of the following important characteristics. The transport of the atoms is in the quantum regime, where all atoms are in the vibrational ground state of the lattice. With our setup mechanical noise is avoided and we achieve precise positioning (below the imaging resolution of $1\mu\text{m}$). We demonstrate high transport velocities of up to 6 m/s, which are accurately controlled on the quantum level. At the same time the velocity spread of the atoms is not more than 2 mm/s, corresponding to 1/3 of a photon recoil.

Horizontal transport of atoms over larger distances holds two challenges: how to move the atoms and how to support them against gravity. Our approach here is to use a novel 1D optical lattice trap, which is formed by a Bessel laser beam and a counterpropagating

Gaussian beam. The Bessel beam leads to radial confinement holding the atoms against gravity. By detuning the laser beams relatively to each other the lattice moves the atoms along the axial direction.

This thesis is divided into three main chapters. Chapter 2 is an introduction into Gaussian and Bessel laser beams and optical lattices. Chapter 3 discusses different theoretical approaches of how to treat and understand the dynamics of atoms in moving optical lattices. Here, we mainly focus on the acceleration process. Finally, in chapter 4 we present in detail the transport experiments and discuss the results.

Appendix A describes the self built digital radio-frequency synthesizers which controlled the lattice motion. Appendix B describes another project of my diploma thesis which is not directly connected to the transport experiments. Here, the set up of a phase stable frequency lock between two diode lasers is described.

2. The optical lattice

In our experiment the atoms are trapped in a standing wave of light, formed by two lasers, which are detuned far off resonance. In the first section of this chapter the most important features of this trapping force are presented. Then possible laser fields, in particular the Bessel beams, are introduced. Their ideal behavior as well as the ideas of how to produce them in the laboratory are discussed. Eventually it is shown, how a Bessel beam together with a Gaussian beam can be used to generate an optical lattice.

2.1. The dipole potential

The optical dipole force [Gri00, Met99], also known as the gradient force or the reactive force, relies on absorption and *stimulated emission* processes. Today it is widely used to form traps for neutral atoms. Unlike radiative traps, dipole traps are operated with light far detuned from the atomic resonances.

In the semiclassical picture this dipole force arises from the interaction between the induced atomic dipole moment \vec{p}_e and the classical electric field.

$$\mathbf{F}_{\text{dip}}(\mathbf{r}) = -\nabla U_{\text{dip}}(\mathbf{r}) \quad (2.1)$$

$$\begin{aligned} U_{\text{dip}}(\mathbf{r}) &= -\frac{1}{2} \overline{\mathbf{p}_e \mathbf{E}} = -\frac{1}{2} \overline{\alpha \mathbf{E}^2} \\ &= -\frac{1}{2\epsilon_0 c} \text{Re}(\alpha) I(\mathbf{r}) \end{aligned} \quad (2.2)$$

where the horizontal bars denote the average over the rapid oscillations of the optical field, α the atomic polarizability and $I(\mathbf{r})$ the intensity of the light field.

The polarizability may be calculated quantummechanically and turns out to depend decisively on the atomic level structure [CT99].

In the case of trapping Rb-atoms, only the transitions from the $5S_{1/2}$ to the $5P_{1/2}$ (D1-line) and from the $5S_{1/2}$ to the $5P_{3/2}$ (D2-line) are relevant. The potential may be written as

$$U_{\text{dip}}(\mathbf{r}) = -\frac{\pi c^2 \Gamma}{2\omega_0^3} \left(\frac{1}{\omega_1 - \omega} + \frac{1}{\omega_1 + \omega} + \frac{2}{\omega_2 - \omega} + \frac{2}{\omega_2 + \omega} \right) I(\mathbf{r}) \quad (2.3)$$

where Γ is the total decay rate from the P-levels, $\omega_{1,2}$ the transition frequencies of the D-lines and $\omega_0 = (\omega_1 + \omega_2)/2$ the mean transition frequency of the two D-lines. The transition wavelengths are $2\pi c/\omega_1 = 795 \text{ nm}$ and $2\pi c/\omega_2 = 780 \text{ nm}$ and the relative strength of the lines are $1/3$ and $2/3$, respectively.

In general the detuning of the dipole beams is much larger than the linewidth of the relevant transitions ($\omega_{1,2} - \omega \gg \Gamma$), so that the atoms stay mostly in the ground state $|i\rangle$. Moreover in most experiments the detuning is chosen such that further approximations can be made. Firstly the second and the fourth term in equation (2.3), the so-called counterrotating terms can be neglected as long as the detuning stays small compared to the laser frequency itself ($\omega_{1,2} - \omega \ll \omega$). Neglecting those terms is known in the literature as the rotating wave approximation (RWA). Secondly if the detuning does not only exceed the linewidth, but also the fine structure splitting ($\omega_{1,2} - \omega \gg \omega_2 - \omega_1$), it is sensible to introduce an effective mean detuning.

$$U_{\text{dip}}(\mathbf{r}) = -\frac{\pi c^2}{2\omega_0^3} \frac{\Gamma}{\Delta} I(\mathbf{r}) \quad (2.4)$$

where the effective detuning Δ is given by

$$\Delta = \frac{3\Delta_1\Delta_2}{2\Delta_1 + \Delta_2} \quad \Delta_{1,2} = \omega_{1,2} - \omega. \quad (2.5)$$

Our trapping laser is operated at a wavelength of $\lambda = 2\pi c/\omega = 830$ nm. The resulting effective mean detuning is $\Delta = 2\pi \times 20$ THz.

Although optical dipole traps are operated off-resonance, residual spontaneous emission processes occur, that can lead to heating of the atomic sample or a loss of trapped atoms. For this reason another important quantity for dipole trapping is the *photon scattering rate* [Gri00].

$$\Gamma_{\text{scatt}} = \frac{\pi c^2}{2\hbar\omega_0^3} \left(\frac{\Gamma}{\Delta}\right)^2 I(\mathbf{r}) \quad (2.6)$$

Typically one has to keep $1/\Gamma_{\text{scatt}}$ small compared to time scale of the experiment, in order to keep the probability for a spontaneous emission process low. Deriving the ratio

$$\frac{\hbar \Gamma_{\text{scatt}}}{U_{\text{dip}}} = \frac{\Gamma}{\Delta} \quad (2.7)$$

shows, for a fixed trap depth U_{dip} the scattering rate decreases for increasing detuning; i.e. in principle the scattering rate can be made arbitrarily small. The drawback of course is, that for larger detunings more power is needed to achieve the same trap depth.

2.2. Laser beams

In charge- and currentfree space the Maxwell equations [Jac02] lead to a wave equation for the electromagnetic fields $\mathbf{E}(\mathbf{r}, t)$ and $\mathbf{B}(\mathbf{r}, t)$. This so-called Helmholtz equation reads

$$\Delta E_i(\mathbf{r}) + k_i^2 E_i(\mathbf{r}) = 0 \quad (2.8)$$

with the dispersion relation $k_i^2 = \frac{\omega_i^2}{c^2}$, $i = \{x, y, z\}$.

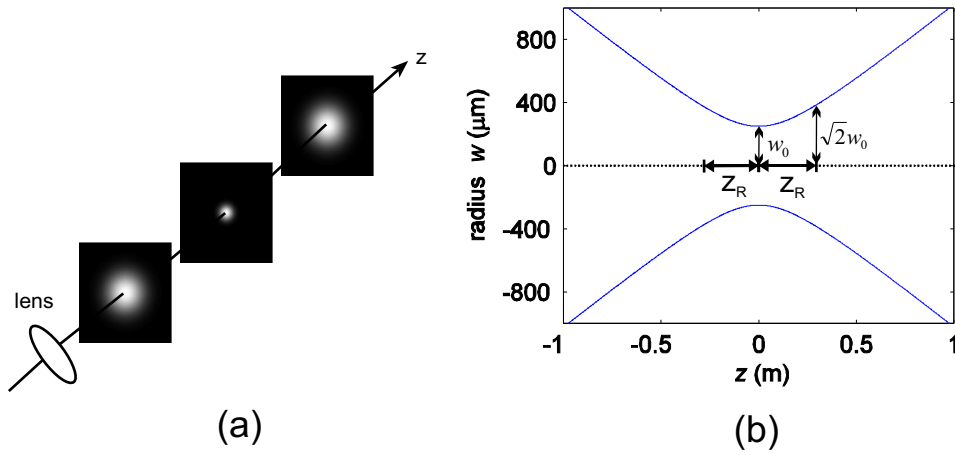


Figure 2.1.: (a) Schematic of a Gaussian beam; e.g. generated by focussing with an ordinary spherical lens. (b) The radius of a Gaussian Beam with a wavelength of $\lambda = 780 \text{ nm}$ and a waist of $w_0 = 250 \mu\text{m}$ is shown as a function of the distance from the focal point $z(\text{m})$. The resulting Rayleigh-range is $z_R = \pi w_0^2 / \lambda = 25 \text{ cm}$.

2.2.1. Gaussian beams

Solving (2.8) within the paraxial approximation $\{k_x, k_y\} \ll k_z$ leads to the field distribution of a linearly polarized Gaussian beams [Kle89].

$$E_{\text{Gauss}}(r, z) = E_0 \frac{w_0}{w(z)} \exp \left[-\frac{r^2}{w^2(z)} + i \left(\frac{k w_0^2}{2z} \frac{r^2}{w^2(z)} + \arctan \frac{z}{z_R} \right) \right] e^{ikz} \quad (2.9)$$

$$\begin{aligned} k &= \frac{2\pi}{\lambda} \\ w(z) &= w_0 \sqrt{1 + \frac{z^2}{z_R^2}} \\ z_R &= \frac{\pi w_0^2}{\lambda} \end{aligned}$$

where λ is the wavelength, w_0 the waist, $w(z)$ the radius and z_R the Rayleigh range of the beam. For our further analysis, it is sufficient to continue with a simplified version

$$E_{\text{Gauss}}(r, z) = E_0 \frac{w_0}{w(z)} \exp \left[-\frac{r^2}{w^2(z)} + ikz \right] \quad (2.10)$$

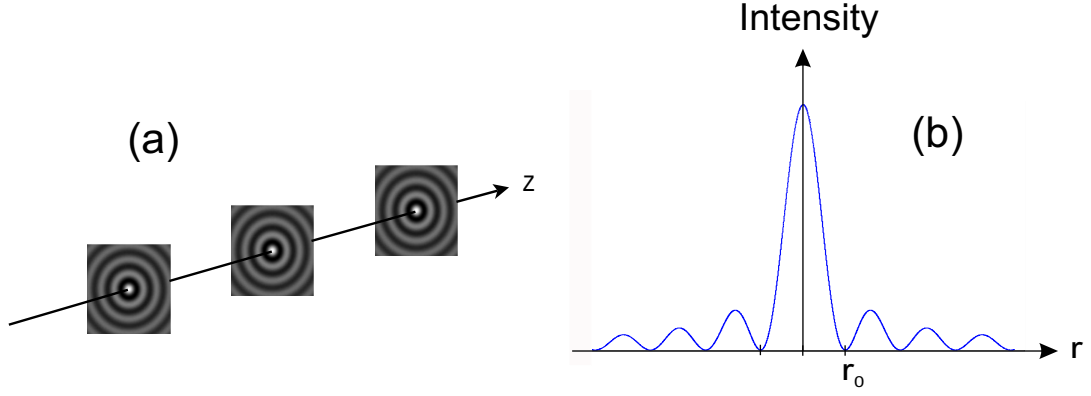


Figure 2.2.: Schematic of a Bessel beam: The intensity of an ideal Bessel beam, given by equation (2.13), is independent of the axial position z .

where we have neglected the fact, that the wave fronts are curved. The intensity distribution of those beams may in any case be written as

$$\begin{aligned}
 I_{\text{Gauss}}(r, z) &= \frac{1}{2} c \epsilon_0 |E_{\text{Gauss}}|^2 \\
 &= \frac{2P}{\pi w_0^2 \left(1 + \frac{z^2}{z_R^2}\right)} \exp \left[\frac{-2r^2}{w_0^2 \left(1 + \frac{z^2}{z_R^2}\right)} \right]
 \end{aligned} \tag{2.11}$$

where P is the total power of the beam.

2.2.2. Bessel beams

In 1987 Durnin and Co-workers found another interesting solution to the Helmholtz equation (2.8). The field is given by [Dur87a, Dur87b]

$$\begin{aligned}
 E(r, \varphi, z) &= E_0 \cdot e^{i\beta z} e^{il\varphi} J_l(\alpha r) \quad l \in \mathbb{Z} \\
 \alpha^2 + \beta^2 &= k^2 = \left(\frac{\omega}{c}\right)^2
 \end{aligned} \tag{2.12}$$

where $J_l(\alpha r)$ is the l -th order Bessel function of the first kind. The beam is characterized by the parameters α and β . It is important to note, that the expression (2.12) is a product of a radial and an axial part; i.e. the radial field distribution *does not* depend on the axial position.

In the following, we restrict the discussion to order $l = 0$, which we have used in the experiment. By taking the absolute square of (2.12) one gets the intensity distribution (Fig. 2.2) given by

$$I(r, z) = I_0 J_0^2(\alpha r), \quad \forall z, \tag{2.13}$$

where α determines the radius r_0 of the central spot via the first zero crossing of $J_0(\alpha r)$

$$r_0 \approx \frac{4.81}{2\alpha}. \tag{2.14}$$

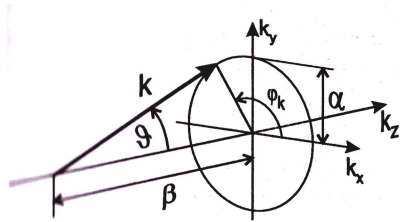


Figure 2.3.: Decomposition of a Bessel beam: The Bessel beam can be seen as a sum of plane waves, whose \mathbf{k} - vectors are lying on the shell of a cone with radius α and height β .

As pointed out before, r_0 and I_0 do not change with the axial position z . Because of this axial independence the Bessel beams are said to be “diffraction-free”. Due to this distinctive feature, a Bessel beam can be used to form a 1D optical lattice with macroscopic axial extension.

Decomposition of a Bessel beam

In cylindrical coordinates the Fourier-transform is given by

$$\tilde{E}(k_{\perp}, \varphi_k, k_z) = \int_0^{\infty} dr r \int_0^{2\pi} d\varphi \int_{-\infty}^{\infty} dz E(r, \varphi, z) e^{-ik_{\perp}r \cos(\varphi - \varphi_k)} e^{-ik_z z} \quad (2.15)$$

Inserting the Bessel field yields to

$$\begin{aligned} &= \int_{-\infty}^{\infty} dz e^{i(\beta - k)z} \int_0^{\infty} dr r J_l(\alpha r) \int_{-\varphi_k}^{2\pi - \varphi_k} d\tilde{\varphi} e^{il\tilde{\varphi} - ik_{\perp}r \cos \tilde{\varphi}} e^{il\varphi_k} \\ &\propto e^{il\varphi_k} \int_{-\infty}^{\infty} dz e^{i(\beta - k)z} \int_0^{\infty} dr r J_l(\alpha r - k_{\perp}r) \\ &\propto e^{il\varphi_k} \delta(k_z - \beta) \frac{\delta(k_{\perp} - \alpha)}{\alpha} \end{aligned} \quad (2.16)$$

Equation (2.16) shows that a Bessel beam is a superposition of plane waves with $(k_{\perp}, k_z) = (\alpha, \beta)$ i.e. the \mathbf{k} - vectors of these plane waves are forming a cone (see Fig.2.3).

2.2.3. Generation of Bessel Beams

First we want to start with a more general treatment of how one may calculate the intensity distribution behind an arbitrary thin and radially symmetric optical element with transmission function $t(r)$ and radius R (Fig. 2.4). In the literature this is known as Kirchhoff’s scalar diffraction theory [Hec05].

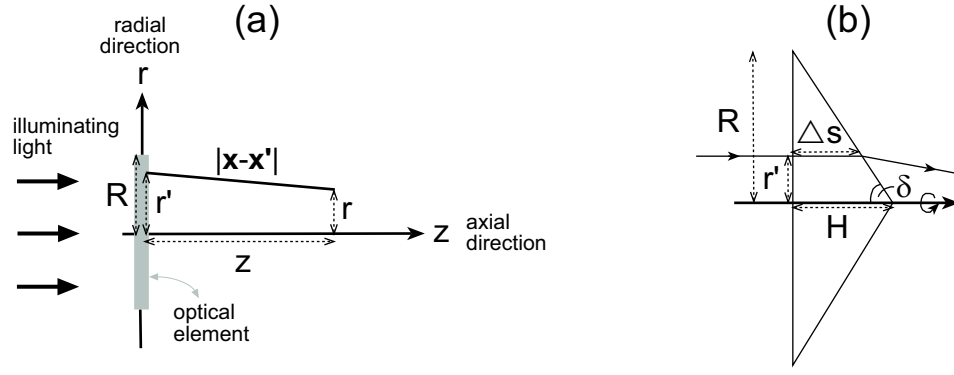


Figure 2.4.: (a) Deriving the field distribution $E(r, z)$ behind an arbitrary optical element of radius R . (b) A light ray passing the refractive axicon at a radial distance r' from the center: The distance covered within the glass is $\Delta s = (R - r')/\tan \delta$, leading to an optical path difference $\Delta \tilde{s}(r') = (n_G - 1)(R - r')/\tan \delta$ and consequently to a phase shift $k\Delta \tilde{s}(r')$.

We assume that the optical element is illuminated with an ideal plane wave. The electric field can be written as a sum of spherical waves coming from the optical element, which is located in the $z=0$ plane. In cylindrical coordinates $(x, y, z) \rightarrow (r \cos \phi, r \sin \phi, z)$ the monochromatic field (wavelength λ) reads

$$E(r, z) = \frac{E_0}{i\lambda} \int_0^R dr' r' \int_0^{2\pi} d\phi' t(r') \frac{e^{ik|\mathbf{x}-\mathbf{x}'|}}{|\mathbf{x}-\mathbf{x}'|} \quad (2.17)$$

where $r' = 0 \dots R$ and $\phi' = 0 \dots 2\pi$ are the coordinates of the optical element. For the distance $|\mathbf{x} - \mathbf{x}'|$ we can write

$$\begin{aligned} |\mathbf{x} - \mathbf{x}'| &= \sqrt{(x - x')^2 + (y - y')^2 + z^2} \\ &= \sqrt{r^2 + r'^2 + z^2 - 2rr' \cos(\phi - \phi')} \\ &\approx z \left(1 + \frac{r^2}{2z^2} + \frac{r'^2}{2z^2} - \frac{rr'}{z^2} \cos(\phi - \phi') \right) \end{aligned} \quad (2.18)$$

Here we have performed a Taylor expansion, valid for $r \ll z$ and $r' \ll z$. Plugging (2.18) into (2.17) leads to

$$\begin{aligned} E(r, z) &\approx \frac{E_0}{i\lambda} \frac{1}{z} e^{ik\left(z + \frac{r^2}{2z^2}\right)} \int_0^R dr' r' t(r') e^{ik\frac{r'^2}{2z^2}} \int_0^{2\pi} d\phi' e^{-k\frac{rr'}{z} \cos(\phi - \phi')} \\ &\approx \frac{E_0}{i\lambda} \frac{1}{z} e^{ik\left(z + \frac{r^2}{2z^2}\right)} \int_0^R dr' r' t(r') e^{ik\frac{r'^2}{2z^2}} 2\pi J_0\left(\frac{rr'}{z} k\right) \end{aligned} \quad (2.19)$$

Refractive axicons

One possibility to produce Bessel-like beams is to use a conical lens, a so-called refractive axicon (Fig. 2.5). Assuming negligible reflection and absorption as well as a small

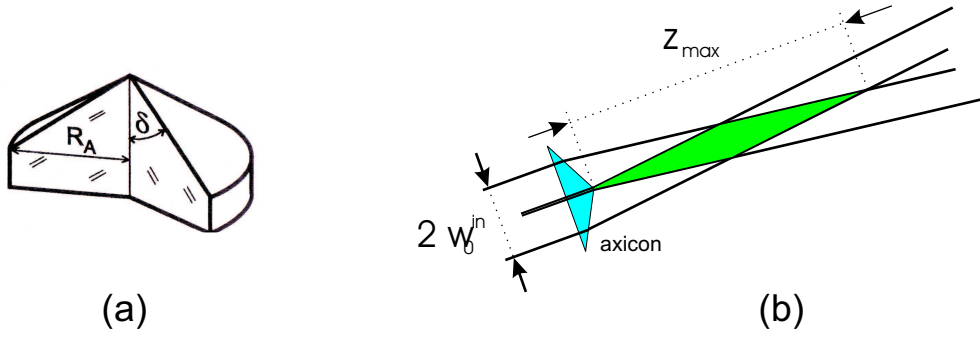


Figure 2.5.: (a) Refractive axicon: a conically-shaped lens characterized by the radius R_A and the apex-angle δ . (b) Geometrical optics picture: A Bessel beam is formed, where the light rays of different directions cross each other. This region has an extension z_{max} , which increases linearly with the radius of the incoming beam w_0^{in} .

axicon height $H \ll z$, the transmission function has the form

$$t(r') = e^{ik\Delta\tilde{s}(r')}. \quad (2.20)$$

The optical path difference $\Delta\tilde{s}(r')$ arises from the fact, that the light passes through glass (index of refraction n_G) instead of air (index of refraction $n \approx 1$) for a distance $\Delta s(r')$ (Fig. 2.4). Given the apex angle of the axicon δ (see Fig. 2.5), the optical path difference

$$\Delta\tilde{s}(r') = (n_G - 1) \frac{R - r'}{\tan \delta} \quad (2.21)$$

and thus the transmission function

$$t(r') = e^{ik(n_G-1)\frac{(R-r')}{\tan\delta}} \rightarrow e^{-ik(n_G-1)\frac{r'}{\tan\delta}} \quad (2.22)$$

may be calculated. In the right hand side of equation (2.22) the constant term $e^{ik(n_G-1)R/\tan\delta}$ is omitted, since the absolute square of this term, which is the relevant quantity for the intensity distribution, equals unity.

By plugging (2.22) into (2.19) we can now calculate the field distribution behind the axicon. The integral can be derived approximately with the method of stationary phase [Vas90, Nig97].

$$I(r, z) \propto z \cdot |J_0(\alpha r)|^2, \quad 0 < z < z_{\text{max}} \quad (2.23)$$

where α is determined by the apex angle δ and the index of refraction n_G of the axicon as well as the wavevector $k = 2\pi/\lambda$ of the laser light.

$$\alpha = k \frac{(n_G - 1)}{\tan \delta} \quad (2.24)$$

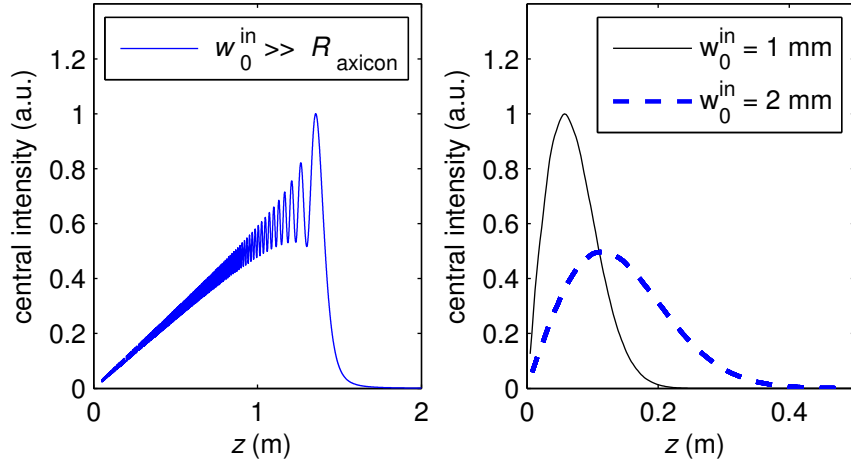


Figure 2.6.: The intensity of the central spot as a function of distance z from the axicon. **(a)** Here $w_0^{\text{in}} \gg R_A = 25.4$ mm, i.e. the axicon is illuminated homogeneously. The oscillations are a consequence of aperturing the beam. **(b)** Here the radius of the incident beam is $w_0^{\text{in}} = 1$ cm and $w_0^{\text{in}} = 2$ cm, respectively. With this choice w_0^{in} is much smaller than R_A and consequently aperture effects are avoided.

Using equation (2.14) the radius of the inner spot may be calculated

$$r_0 = \frac{4.81}{2k(n_G - 1)} \tan \delta. \quad (2.25)$$

The finite axial extension (Fig. 2.5(b)) of the Bessel beam is given by

$$z_{\text{max}} = \frac{R_A \tan \delta}{n_G - 1} \quad (2.26)$$

As seen from equation (2.23) and Fig. 2.6 the intensity of an axicon beam is not independent of the axial position. But the radial distribution and therefore the value for r_0 remain constant within $0 < z < z_{\text{max}}$, as in the case of an ideal Bessel beam.

In our experiments the axicon is not illuminated homogeneously but with a Gaussian beam of waist w_0^{in} . To account for this, we modify the transmission function accordingly.

$$t(r') = e^{-ik(n_G-1)\frac{r'}{\tan \delta}} e^{-\frac{r'^2}{2(w_0^{\text{in}})^2}} \quad (2.27)$$

The parameter α and consequently the radius r_0 of the inner spot stay the same as for the homogeneous illumination. However, the axial intensity distribution and in particular the range of the beam z_{max} now depend on the waist of the incoming beam

$$z_{\text{max}} \simeq \frac{w_0^{\text{in}} \tan \delta}{n_G - 1}. \quad (2.28)$$

The intensity distribution itself may be calculated numerically. In Fig. 2.6(b) it is shown for two different sizes w_0^{in} of the impinging beam.

In summary refractive axicons may be used to create Bessel-like beam quite efficiently. The only drawback is, that refractive axicons with a tip of decent quality seem to be hard to produce¹.

Diffractive axicons

Diffractive axicons are circular symmetric diffraction gratings (Fig. 2.7(a)). For ideally blazed gratings, whose height h is a multiple of the laser wavelength $\lambda = 2\pi/k$, the transmission function equals the transmission function of the refractive axicon. The angle δ is then given by the blazing angle of the grating.

Well blazed circular-symmetric gratings are hard to fabricate. Thus the grooves of commonly produced diffractive axicons do not have a smooth triangular shape, but are cascaded. The simplest version of such a grating is a binary one (Fig. 2.7(b)). It is fairly easy to produce, however, the Bessel beam only contains approximately 40% of the power of the illuminating beam. The rest of the light has to be filtered out [Vas90] and cannot be used for the experiment. For typical gratings (4-step gratings) produced nowadays the efficiency is around 80%.

We decided to not use diffraction gratings, because the generation efficiency is always less than for refractive axicons (unity efficiency). Furthermore no filtering is necessary for refractive axicons.

However, diffractive axicons in general have the advantage, that also Bessel beams of higher orders may be produced. By providing blue-detuned light, this enables for instance to generate a light tube of macroscopic extent.

2.3. Standing wave potentials

2.3.1. Gaussian beam lattice

One-dimensional standing wave traps are typically formed by two counterpropagating Gaussian beams with identical waists and focal points. The atoms are trapped close to the center, where $z \ll z_R$ and $r \ll w_0$. In this regime the expression for the field of the Gaussian beam (2.10) may be further simplified

$$E_{\text{Gauss}}(r, z) = E_0 e^{ikz} \left(1 - \frac{r^2}{w_0^2} \right) \quad (2.29)$$

¹All together we got three axicons from Del Mar Photonics. However, only one of those three produced a beam useable for our experiments. Asymmetries as well as several dots instead of concentric rings were observed, when illuminating the other two axicons.

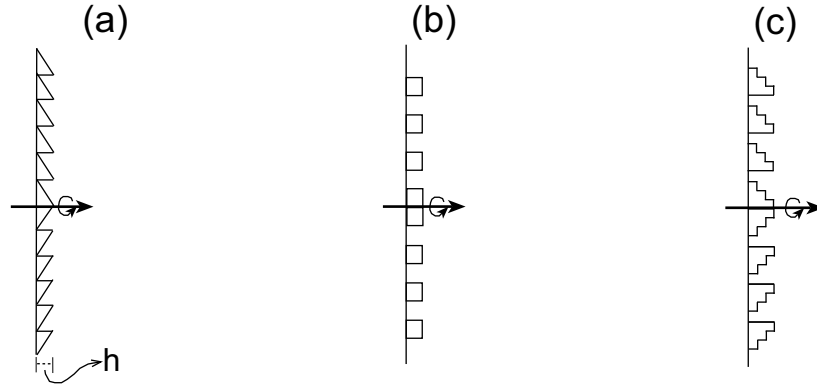


Figure 2.7.: **(a)** A circular-symmetric blazed diffraction grating is fully equivalent to an refractive axicon, in case the laser wavelength $\lambda = 2\pi/k$ is a multiple of nh , where n is the index of refraction of the grating and h the height as indicated. **(b)** A circular-symmetric binary diffraction grating. **(c)** A circular-symmetric four-step grating.

leading to a standing wave intensity pattern given by

$$\begin{aligned} I(r, z) &= \left| \sqrt{I_1} e^{ikz} + \sqrt{I_2} e^{-ikz} \right|^2 \left(1 - \frac{r^2}{w_0^2} \right)^2 \\ &= \left(I_1 + I_2 + 2\sqrt{I_1 I_2} \cos 2kz \right) \left(1 - \frac{r^2}{w_0^2} + \mathcal{O}\left(\frac{r^4}{w_0^4}\right) \right) \end{aligned} \quad (2.30)$$

with $I_{1,2} = 2P_{1,2}/(\pi w_0^2)$ being the central intensities and $P_{1,2}$ the total powers of the two counterpropagating beams. Plugging the intensity distribution (2.30) into equation (2.4) and substituting $\cos(2kz) = 1 - 2\sin^2(kz)$ leads to the lattice potential

$$U(r, z) = (-U_0 + U_{\text{latt}} \sin^2 kz) \left(1 - \frac{2r^2}{w_0^2} \right). \quad (2.31)$$

where the total trap depth U_0 and the modulation depth of the lattice part of the potential U_{latt} are given by

$$U_0 = \frac{\pi c^2}{2\omega_0^3} \frac{\Gamma}{\Delta} \left(I_1 + I_2 + 2\sqrt{I_1 I_2} \right) \quad (2.32)$$

$$U_{\text{latt}} = \frac{\pi c^2}{2\omega_0^3} \frac{\Gamma}{\Delta} 4\sqrt{I_1 I_2} \quad (2.33)$$

In the special case, when the two beams have equal intensities $I_1 = I_2 = I_0$ (when e.g. a retro-reflecting mirror is used), $U_0 = U_{\text{latt}}$ the potential reads $U(r, z) = -U_0 \left(1 - 2r^2/w_0^2 \right) \cos^2 kz$ with $U_0 = \frac{\pi c^2}{2\omega_0^3} \frac{\Gamma}{\Delta} 4I_0$.

In order to describe how tight the atoms are confined, the trap frequencies are derived. By making a quadratic approximation for both directions, we get

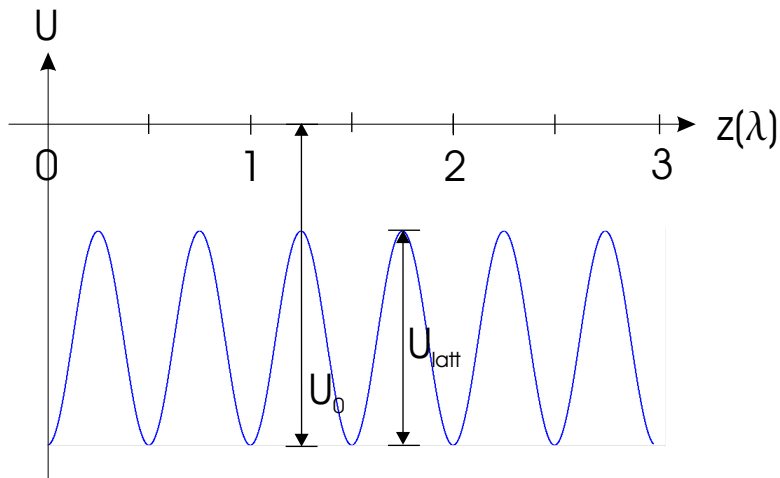


Figure 2.8.: Illustration of the total trap depth U_0 and the modulation depth U_{latt} . The potential $U(r=0, z)$ is shown as a function of z . Interestingly for a Gaussian beam lattice the ratio U_{latt}/U_0 stays the same for $r \neq 0$, as can be seen from equation (2.31). For a Bessel-Gauss lattice, however, the situation is more involved (equation (2.37)) and U_0 and U_{latt} are indeed only representable parameters for $r = 0$.

$$\begin{aligned}\omega_r &= 2\pi\nu_r = \sqrt{\frac{4U_0}{mw_0^2}} \\ \omega_z &= 2\pi\nu_z = k\sqrt{\frac{2U_{\text{latt}}}{m}}\end{aligned}\quad (2.34)$$

2.3.2. Bessel-Gauss lattice

For our long distance transport experiments a standing wave formed by a Bessel beam and a counterpropagating Gaussian beam (Bessel-Gauss lattice) is used.

The Bessel beam with radius $r_0 = 4.81/(2\alpha)$ confines the atoms along the radial direction and supports them against gravity. For the lattice confinement along the axial direction a counterpropagating Gaussian beam with a large waist $w_0 \gg r_0$ is used. For the trapping region $r \ll r_0 \ll w_0$ we may write

$$\begin{aligned}E_{\text{Bessel}}(r, z) &= E_B e^{ikz} \left(1 - \frac{(\alpha r)^2}{8}\right) \\ E_{\text{Gauss}}(r, z) &= E_G e^{ikz}\end{aligned}\quad (2.35)$$

The resulting interference pattern reads

$$\begin{aligned} I(r, z) &= \left| \sqrt{I_B} e^{ikz} \left(1 - \frac{(\alpha r)^2}{8} \right) + \sqrt{I_G} e^{-ikz} \right|^2 \\ &= I_B \left(1 - \frac{(\alpha r)^2}{4} + \mathcal{O}(r^4) \right) + I_G + 2\sqrt{I_B I_G} \left(1 - \frac{(\alpha r)^2}{8} \right) \cos(2kz) \end{aligned} \quad (2.36)$$

where I_B is the central intensity of the Bessel beam and I_G the central intensity of the Gaussian beam. The resulting potential is given by

$$\begin{aligned} U(r, z) = & - U_0 \left[\frac{I_B}{(\sqrt{I_B} + \sqrt{I_G})^2} \left(1 - \frac{(\alpha r)^2}{4} \right) + \frac{I_G}{(\sqrt{I_B} + \sqrt{I_G})^2} \right. \\ & \left. + \frac{2\sqrt{I_B I_G}}{(\sqrt{I_B} + \sqrt{I_G})^2} \left(1 - \frac{(\alpha r)^2}{8} \right) \right] + U_{\text{latt}} \left(1 - \frac{(\alpha r)^2}{8} \right) \sin^2 kz \end{aligned} \quad (2.37)$$

with the total trap depth U_0 and the modulation depth U_{latt} being defined analogous to (2.33)

$$U_0 = \frac{\pi c^2}{2\omega_0^3} \frac{\Gamma}{\Delta} \left(I_B + I_G + 2\sqrt{I_B I_G} \right) \quad (2.38)$$

$$U_{\text{latt}} = \frac{\pi c^2}{2\omega_0^3} \frac{\Gamma}{\Delta} 4\sqrt{I_B I_G}. \quad (2.39)$$

The resulting trap frequencies are

$$\begin{aligned} \omega_r &= 2\pi\nu_r = \sqrt{\frac{1}{m} \left(\frac{\partial^2}{\partial r^2} U(z=0) \right)_{r=0}} = \sqrt{\frac{U_0 \alpha^2}{2m} \frac{I_B + \sqrt{I_B I_G}}{(\sqrt{I_B} + \sqrt{I_G})^2}} \\ \omega_z &= 2\pi\nu_z = \sqrt{\frac{1}{m} \left(\frac{\partial^2}{\partial z^2} U(r=0) \right)_{z=0}} = k \sqrt{\frac{2U_{\text{latt}}}{m}} \end{aligned} \quad (2.40)$$

Again, in the case of equal intensities $I_B = I_G = I_0$ we have $U_0 = U_{\text{latt}}$. The potential may then be written as

$$U(r, z) = -U_0 \left(1 - \frac{(\alpha r)^2}{8} \right) \cos^2 kz \quad (2.41)$$

$$\begin{aligned} \omega_r &= 2\pi\nu_r = \sqrt{\frac{U_0 \alpha^2}{4m}} \\ \omega_z &= 2\pi\nu_z = k \sqrt{\frac{2U_0}{m}} \end{aligned} \quad (2.42)$$

As we have seen in the previous section, the center intensity I_B of non-ideal Bessel beams, such as the axicon beams in our experiment, also varies with the axial position. However, as mentioned before, I_B can be made sufficiently constant over a principally arbitrary range, assuming, that there is enough power available.

3. Atoms in moving lattices

In this chapter several ways to understand the behavior of a cold atomic cloud in a moving optical lattice are presented. A simple classical picture is introduced in the first section. Within the quantum optics approach presented in the second section the problem is treated as a two-level atom interacting with two counterpropagating laser fields of frequencies ω_1 and ω_2 , respectively. Such laser fields describe a moving optical lattice, whose velocity is proportional to the difference between ω_1 and ω_2 . In this context Raman transitions to higher momentum states are the explanation for the acceleration of the atoms [Pei97]. In the third section the more common “solid state - like theory” of particles in a periodic potential is discussed [Dah96, Pei97, Den02]. First of all the stationary eigenvalues and eigenfunctions, the so-called Bloch waves are derived. Then a constant force term is added to the Hamiltonian, representing a constant acceleration of the lattice. Eventually the problem of instabilities, arising from the combination of interatomic interactions plus an external lattice potential, is discussed.

3.1. Moving lattices - Classical approach

In a simple classical picture the atoms are viewed as point-like masses. Since they are sitting in the potential wells of a standing wave potential, they may be dragged along with such an accelerated lattice. However, they will not stay right in the center of the standing wave node, but will move slightly backwards, due to their inertia (Fig. 3.1). More precisely they will move to the axial position z , where the confining force F_z equals

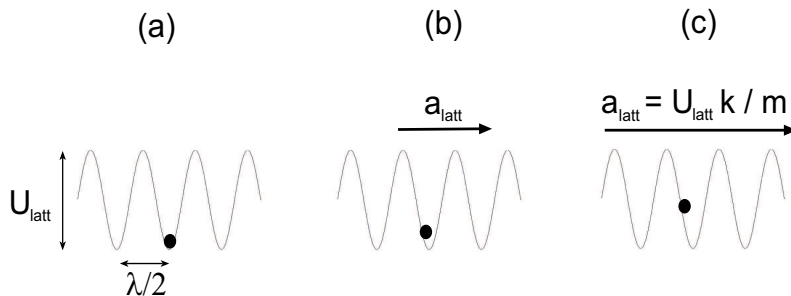


Figure 3.1.: (a): Particle in a lattice at rest. (b) and (c): Particle in an accelerated lattice. For $a_{\text{latt}} > U_{\text{latt}}k/m$ the atoms do not stay in the initial well and can therefore not be dragged along with the lattice.

ma_{latt} , with

$$F_z = -\frac{\partial}{\partial z} U_{\text{latt}} \cos^2(kz) \quad (3.1)$$

$$= U_{\text{latt}} k \sin(2kz). \quad (3.2)$$

and a_{latt} being the acceleration of the lattice. This axially confining force has a maximum value of

$$F_{z,\text{max}} = U_{\text{latt}} k. \quad (3.3)$$

In order to keep an atom bound to the lattice, we thus require the acceleration a to be small enough such that

$$ma_{\text{latt}} < U_{\text{latt}} k. \quad (3.4)$$

As we will see later, this upper limit on the acceleration arising from classical considerations, is appropriate in the case of deep lattices ($U_{\text{latt}} \gg E_r$).

3.2. Moving lattices - Quantum optics approach

3.2.1. Transfer between momentum states

The state of an atom may generally be described by its internal state and its total momentum p . In the case of a two level atom the total energy of this state is then given by

$$E = E_{g,e} + \frac{p^2}{2m} \quad (3.5)$$

Thus the energy diagram $E(p)$ consists of two parabolas with an offset given by E_g and E_e , respectively (Fig. 3.2).

In a proper electromagnetic field the atoms are stimulated to absorb and emit photons. Through these processes a discrete amount of energy and momentum is transferred to the atom. For a single photon absorption or photon emission event an energy of $\hbar\omega$ and a momentum of $\hbar k$ is exchanged.

Our goal is to accelerate the atoms; that is to transfer them from the zero momentum state $|g, 0\rangle$ to a state $|g, 2N\hbar k\rangle$ with a large number N . This goal is achieved by consecutively driving Raman transitions between a state $|g, 2(n-1)\hbar k\rangle$ and state $|g, 2n\hbar k\rangle$, where $n = 1, 2, \dots, N$. Assuming that one laser is kept at constant frequency ω_1 , the n -th Raman resonance is hit by tuning the second laser to

$$\omega_2^{(n)} = \omega_1 - 4(2n-1)\omega_r. \quad (3.6)$$

where $E_r = \hbar\omega_r = \frac{(\hbar k)^2}{2m}$ is the recoil energy.

One possibility to transfer all the atoms into the state $|g, 2N\hbar k\rangle$ is applying N light pulses (so-called Rabi- π -pulses), where the frequencies of the laser beams are tuned to ω_1 and $\omega_2^{(n=1, \dots, N)}$, respectively. This method, however, is quite demanding, since for a

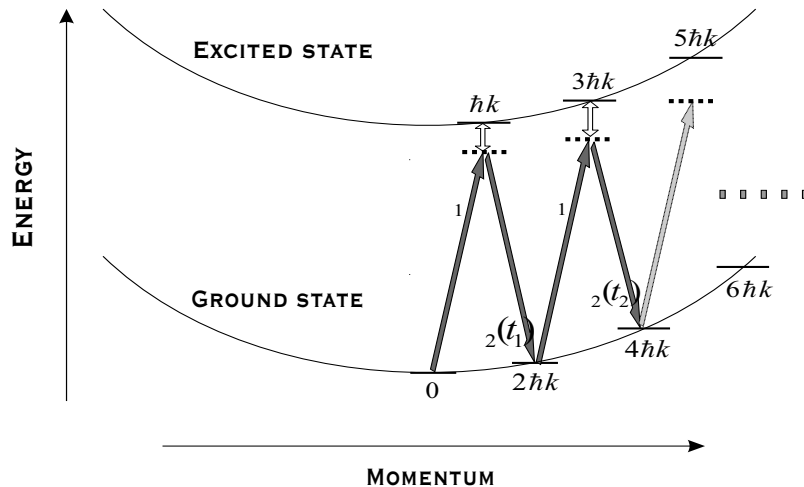


Figure 3.2.: Quantum mechanical picture of the acceleration process: The total energy of the atom is plotted versus momentum. Population transfer into states with higher momentum is achieved by consecutive ARP. This ARP scheme is realized by keeping the frequency of the first laser ω_1 constant and ramping the frequency of the second one linearly $\omega_2 = \omega_1 + \dot{\omega}_2 t$ with $\dot{\omega}_2 < 0$. The n -th avoided crossing is then hit after a time $t_n = 4(2n - 1)\omega_r/\dot{\omega}_2$.

full population transfer both the intensity of the laser and the pulse length have to be well controlled.

An alternative is the adiabatic rapid passage scheme discussed in the following. It is advantageous, because on the one hand it is much less sensitive to fluctuations in the intensity of the light and on the other hand the lasers do not have to be switched.

3.2.2. Adiabatic rapid passage

In order to study the adiabatic rapid passage scheme [Lan32, Zen32, Rab57] in more detail we pick out the first Raman resonance between the state $|g, 0\hbar k\rangle \equiv |\psi_1\rangle$ and the state $|g, 2\hbar k\rangle \equiv |\psi_2\rangle$ (see Fig. 3.3). The common detuning Δ is chosen sufficiently large, so that the excited state $|e, \hbar k\rangle$ is basically unpopulated. Consequently the three level system shown in Fig. 3.3 may be treated as a quasi-two level system.

In the interaction picture the Hamiltonian of this quasi-two level system may be written as

$$\tilde{H} = \frac{\hbar}{2} \begin{pmatrix} \delta & \Omega \\ \Omega & -\delta \end{pmatrix} \quad (3.7)$$

where $\delta = \omega_1 - \omega_2 - (E_2 - E_1)$ is the detuning from the Raman resonance. The effective Rabi frequency Ω is given by

$$\Omega = \frac{\Omega_1 \Omega_2}{2\Delta} \quad (3.8)$$

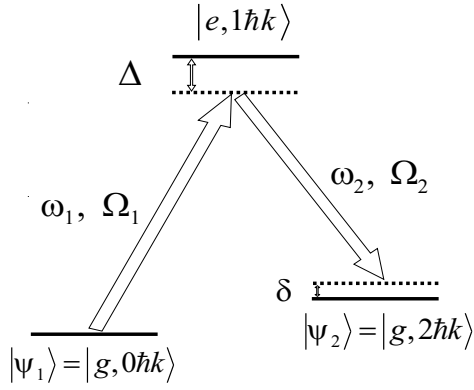


Figure 3.3.: The “lambda system”: A Raman transition from $|\psi_1\rangle$ to $|\psi_2\rangle$ may be driven via a virtual state in the vicinity of state $|e, 1\hbar k\rangle$. A large Δ is needed to avoid spontaneous emission from $|e, 1\hbar k\rangle$. For ARP ω_2 and consequently δ is changed adiabatically.

where the Rabi frequencies Ω_1 and Ω_2 are determined by the intensity of the two beams as well as the coupling between the internal states of the atom. The two dimensional unity vectors $\begin{pmatrix} 1 \\ 0 \end{pmatrix}$ and $\begin{pmatrix} 0 \\ 1 \end{pmatrix}$ correspond to the eigenstates $|\tilde{\psi}_1\rangle$ and $|\tilde{\psi}_2\rangle$ in the interaction picture, i.e.

$$\begin{aligned} \begin{pmatrix} 1 \\ 0 \end{pmatrix} &\doteq |\tilde{\psi}_1\rangle \\ \begin{pmatrix} 0 \\ 1 \end{pmatrix} &\doteq |\tilde{\psi}_2\rangle \end{aligned} \quad (3.9)$$

As seen from equation (3.7), the total Hamiltonian in this rotating basis (interaction picture) is time-independent. Therefore stationary eigenvalues and eigenvectors exist

$$\begin{aligned} \tilde{E}_{\pm} &= \pm \frac{\hbar}{2} \sqrt{\Omega^2 + \delta^2} \\ |\tilde{\psi}_+\rangle &= \cos \theta |\tilde{\psi}_1\rangle + \sin \theta |\tilde{\psi}_2\rangle \\ |\tilde{\psi}_-\rangle &= -\sin \theta |\tilde{\psi}_1\rangle + \cos \theta |\tilde{\psi}_2\rangle \end{aligned} \quad (3.10)$$

with the so-called mixing angle given by

$$\begin{aligned} \cos \theta &= \sqrt{\frac{1}{2} \left(1 + \frac{\delta}{\sqrt{\Omega^2 + \delta^2}} \right)} \\ \sin \theta &= \sqrt{\frac{1}{2} \left(1 - \frac{\delta}{\sqrt{\Omega^2 + \delta^2}} \right)} \end{aligned} \quad (3.11)$$

Let us now consider a ground state atom in far blue detuned field ($|\delta| \gg \Omega$, $\delta > 0$). Thus the state of the system is

$$|\tilde{\psi}_+\rangle \simeq |\tilde{\psi}_1\rangle \quad (3.12)$$

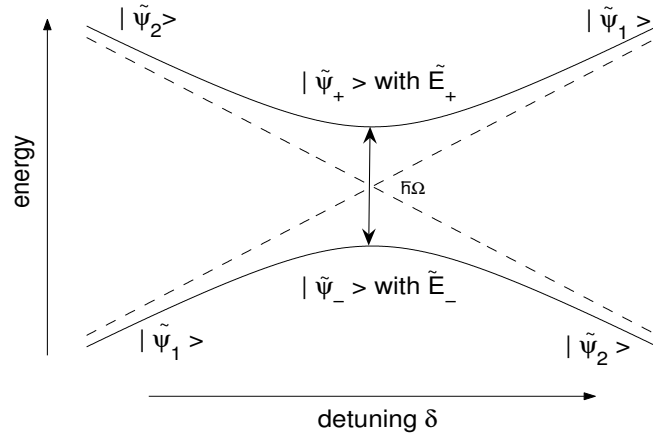


Figure 3.4.: The energies E_{\pm} of the dressed states $|\tilde{\psi}_{+}\rangle$ and $|\tilde{\psi}_{-}\rangle$ is plotted (solid line): The dashed line shows the asymptotic limit for vanishing Rabi-frequency. For a non-zero Rabi frequencies an avoided crossing emerges (arrow). On resonance ($\delta = 0$) the energy splitting between the two levels is $\hbar\Omega$. For large detunings $|\delta| \gg \omega$, the states $|\tilde{\psi}_{\pm}\rangle$ coincide with either $|\tilde{\psi}_{1}\rangle$ or $|\tilde{\psi}_{2}\rangle$.

If we now *slowly* change the detuning, the system will adiabatically follow the changes of the Hamiltonian \tilde{H} ; i.e. it will stay in it's eigenstate $|\tilde{\psi}_{+}\rangle$. The probability for undesired jumps from the $|\tilde{\psi}_{+}\rangle$ to $|\tilde{\psi}_{-}\rangle$ (or vice-versa) is given by the Landau-Zener formula [Lan32, Zen32]

$$P_{\pm \rightarrow \mp} = e^{-\frac{\pi}{2} \frac{\Omega^2}{d\delta/dt}}. \quad (3.13)$$

This probability is vanishing for

$$\frac{d\delta}{dt} \ll \frac{\pi}{2} \Omega^2 \quad (3.14)$$

That means, as long as the adiabaticity criteria (3.14) is fulfilled, the system indeed stays in state $|\tilde{\psi}_{+}\rangle$. In this adiabatic regime the probability of finding the atom in state $|\tilde{\psi}_{2}\rangle$ increases continuously according to

$$\begin{aligned} P_2 &= |\langle \tilde{\psi}_2 | \tilde{\psi}_+ \rangle|^2 = \sin^2 \theta \\ &= \frac{1}{2} \left(1 - \frac{\delta}{\sqrt{\delta^2 + \Omega^2}} \right). \end{aligned} \quad (3.15)$$

Thus, if the laser frequency is adiabatically swept from the far blue detuned across resonance to the far red detuned regime ($|\delta| \gg \Omega$, $\delta < 0$), the final state is

$$|\tilde{\psi}_{+}\rangle \simeq |\tilde{\psi}_{2}\rangle \quad (3.16)$$

i.e. by adiabatically sweeping across resonance the bare state of the atom may be changed from $|\psi_1\rangle \equiv |g, 0\hbar k\rangle$ to $|\psi_2\rangle \equiv |g, 2\hbar k\rangle$

This transfer from the ground to the excited state is called “*adiabatic rapid passage*”.

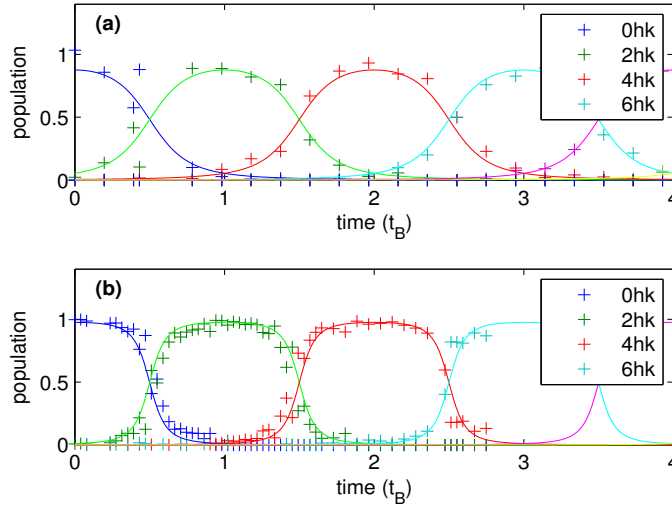


Figure 3.5.: Measurement of the population of the first three momentum states for **(a)** $U_0 = 4.4E_r$ and **(b)** $U_0 = 1.8E_r$: The frequency of the second laser is ramped according to (3.17) for a certain time t . Then both lasers are turned off abruptly and the momentum components are separated by free expansion. The time t is given in units of the Bloch period $t_B = 8\omega_r/\dot{\omega}_2$, which is the time it takes to increase the mean momentum of the cloud by $2\hbar k$.

Consecutive Adiabatic Rapid Passage

We have seen, how the Adiabatic Rapid Passage (ARP) scheme can be used to accelerate the entire BEC to a momentum of $2\hbar k$. By sweeping the laser further, more Raman resonances may be hit and the atoms may be transferred to the $|g, 4\hbar k\rangle$ state, $|g, 6\hbar k\rangle$ state, et cetera. For the measurements presented in this chapter, the second laser is swept linearly ($\dot{\omega}_2 = \text{const.} < 0$)

$$\omega_2(t) = \omega_1 + \dot{\omega}_2 t \quad (3.17)$$

with

$$8\hbar^2\dot{\omega}_2 \ll U_0^2\pi \quad (3.18)$$

in order to avoid Landau-Zener tunneling. Here we have taken equation (3.14), where we have substituted the Rabi frequency by the potential depth $U_0 = 2\hbar\Omega$.

In addition we restrict the discussion for now to lattice depths U_0 , which are small enough, that the extension of the crossing zones, given by $\sim \Omega = U_0/(2\hbar)$, is much smaller than the frequency difference between two crossings

$$\Omega = \frac{U_0}{2\hbar} < 8\omega_r. \quad (3.19)$$

In this case the simple model of ARP for a two-level atom given above can be used to calculate the probability for an atom being in state $|g, 2n\hbar k\rangle$, ($n = 0, 1, 2, \dots$). Using equation 3.15 we get

$$P_{2n\hbar k} = \frac{1}{2} \left(\frac{\delta_n}{\sqrt{\delta_n^2 + \Omega^2}} - \frac{\delta_{n+1}}{\sqrt{\delta_{n+1}^2 + \Omega^2}} \right) \quad (3.20)$$

with the detuning from the respective resonances

$$\begin{aligned} \delta_n &= \omega_2(t) - \omega_2^{(n)} \\ &= \omega_2(t) - \omega_1 + 4\omega_r(2n - 1) \\ &= \dot{\omega}_2 t + 4\omega_r(2n - 1) \end{aligned} \quad (3.21)$$

Thus as a function of time we can write

$$P_{2n\hbar k}(t) = \frac{1}{2} \left(\frac{\dot{\omega}_2 t + 4\omega_r(2n - 1)}{\sqrt{(\dot{\omega}_2 t + 4\omega_r(2n - 1))^2 + \Omega^2}} - \frac{\dot{\omega}_2 t + 4\omega_r(2n + 1)}{\sqrt{(\dot{\omega}_2 t + 4\omega_r(2n + 1))^2 + \Omega^2}} \right) \quad (3.22)$$

For a linear frequency ramp, equation (3.22) gives the population of any momentum state $|g, 2n\hbar k\rangle$ as a function of time. By performing time-of-flight measurements of the cloud after the acceleration process, $P_{2n\hbar k}(t)$ may be measured directly and compared with the calculation. Since condition (3.18) is fulfilled, the predicted curve is in good agreement with the measurements.

Here it should be pointed out, that in order to obtain the result shown in Fig. 3.5, that is to map the state of the atom $|\psi(t)\rangle$ onto the momentum eigenstate basis $|g, 2n\hbar k\rangle$, the laser has to be turned off abruptly after acceleration. Otherwise the atoms might have time to redistribute in momentum space.

Since the majority of the transport measurements, presented in the following are performed at lattice depths of $10E_r$ or less, our model is sufficient to explain the acceleration kinematics in our experiment. And even though our simple picture of consecutive ARP is not appropriate for deep lattices, the physics of the acceleration process does not change significantly.

3.2.3. Mean velocity

For characterizing the movement of the entire cloud the *mean velocity* is derived.

$$\bar{v}(t) = \sum_n \frac{2n\hbar k}{m} P_{2n\hbar k}(t) \quad (3.23)$$

For deep lattices (large Rabi frequencies) the atoms are bound very tightly to potential minima. The mean velocity of the atoms coincides with the speed of the lattice and is therefore also increasing almost linearly with time. When the Rabi frequency is made

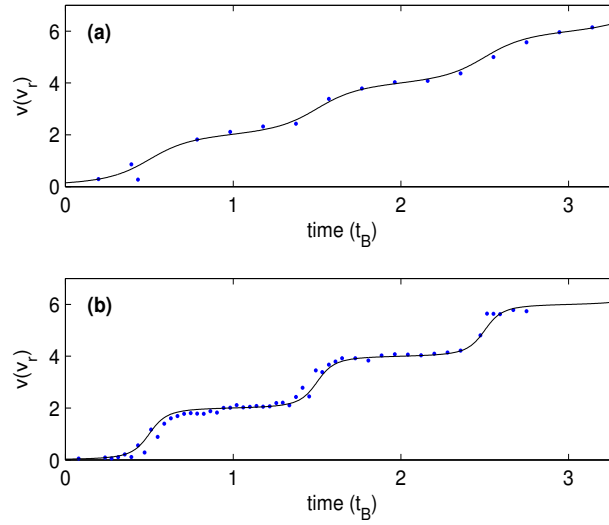


Figure 3.6.: The mean velocity \bar{v} of the cloud as a function of time t for lattice depths of **(a)** $U_0 = 4.4E_r$ and **(b)** $U_0 = 1.8E_r$, respectively. The time t is again given in units of $t_B = 8\omega_r/\dot{\omega}_2$.

smaller, the curve $\bar{v}(t)$ starts to depart from the ideal linear shape (Fig. 3.6). The mean velocity of the atoms in the reference frame of the lattice

$$\bar{v}'(t) = \bar{v}(t) - v_{\text{lattice}}(t) \quad (3.24)$$

is not zero any longer, but shows an oscillatory behavior. These oscillations of $\bar{v}'(t)$ are called Bloch-oscillations and are well known in solid-state physics. They are discussed in more detail in the next section.

3.3. Moving lattices - Solid state physics approach

3.3.1. Band structure

A standing wave formed by two counterpropagating beams with wavelength $\lambda = 2\pi/k$ produces a 1D lattice potential with a periodicity of $\frac{\lambda}{2}$, as we have seen by deriving equation (2.33) and (2.39). Neglecting the constant off-set potential in those equations, we can write the Hamiltonian for a particle in such a potential as

$$H = \frac{p^2}{2m} - U_{\text{latt}} \cos^2 kz \quad (3.25)$$

Since the dynamics of electrons in solids are also described by a Hamiltonian with a periodic potential term, a broad discussion of this type of Hamiltonian and the corresponding Schrödinger equation is found in basically all introductory solid state physics textbooks (see e.g. [Kit87]). Here we want to apply this more general theory to the case of a sinusoidal potential.

By solving the time-independent Schrödinger equation

$$H\phi_{n,q}(z) = E_{n,q}\phi_{n,q}(z) \quad (3.26)$$

the eigenvalues $E_{n,q}$ and -functions $\phi_{n,q}$ are obtained. They are characterized by the band index $n = 1, 2, \dots$ and the quasi-momentum $-\hbar k \leq q \leq \hbar k$. This type of eigenfunctions are called Bloch waves. According to the Bloch theorem [Kit87], they can be rewritten as a product of a plane wave with momentum q and a function $u_{n,q}$ with periodicity $\frac{\lambda}{2}$

$$\phi_{n,q}(z) = e^{iqz/\hbar} u_{n,q}(z) \quad (3.27)$$

This leads to a eigenvalue equation for $u_{n,q}$

$$\left(\frac{(p+q)^2}{2m} - U_0 \cos^2 kz \right) u_{n,q}(x) = E_{n,q} u_{n,q}(x) \quad (3.28)$$

Due to the periodicity we may write $u_{n,q}$ as a Fourier sum

$$u_{n,q}(x) = \sum_l c_l^{n,q} e^{il2kx} \quad (3.29)$$

and the potential as

$$\begin{aligned} U(x) &= -U_0 \cos^2 kz \\ &= -U_0 \left(e^{i2kx} + e^{-i2kx} + 2 \right) \\ &\longrightarrow -U_0 \left(e^{i2kx} + e^{-i2kx} \right) \end{aligned} \quad (3.30)$$

In the last line the constant term was dropped, because it only shifts all the eigenvalues by the same amount and is therefore physically irrelevant.

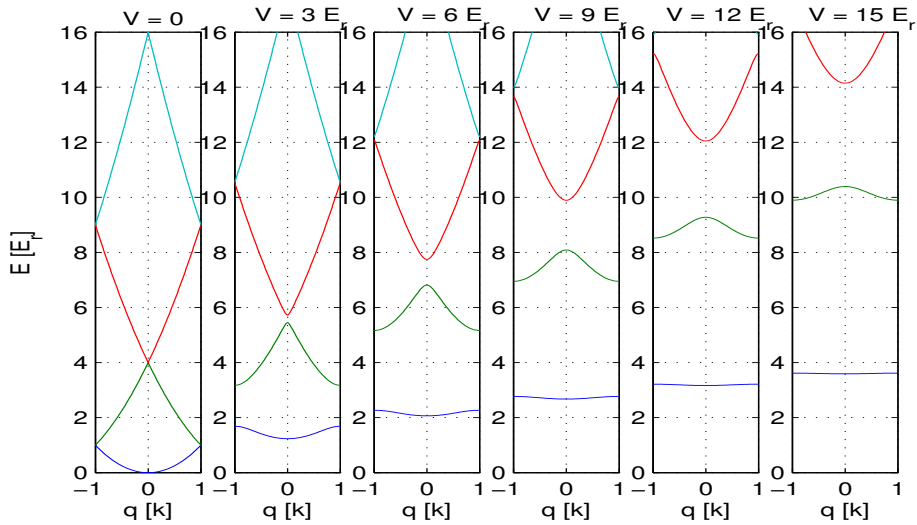


Figure 3.7.: Band structure for different lattice depths U_0 . For $U_0 = 0$ the $E_n(q)$ dependence is parabolic - as expected for a free particle. For very deep lattices on the other hand $E_n(q)$ becomes very flat; i.e. the energy bands turn into energy levels - as expected for a well trapped particle.

Inserting (3.29) and (3.30) into (3.28) leads to

$$\begin{aligned} \sum_l \frac{(2\hbar kl + q)^2}{2m} \cdot e^{il2kx} c_l^{n,q} + \frac{U_0}{4} \left(e^{i2kx(l+1)} + e^{i2kx(l-1)} \right) c_l^{n,q} \\ = \sum_l E_{n,q} e^{il2kx} c_l^{n,q} \end{aligned} \quad (3.31)$$

or equivalently

$$\begin{aligned} \sum_m H_{lm} c_m^{n,q} = E_{n,q} c_l^{n,q} \\ H_{lm} = \begin{cases} (2l + \frac{q}{\hbar k})^2 E_r & \text{if } l = m, \\ -\frac{1}{4} U_0 & \text{if } |l - m| = 1, \\ 0 & \text{else} \end{cases} \end{aligned} \quad (3.32)$$

where $E_r = \frac{(\hbar k)^2}{2m}$ is the recoil energy.

The desired energy eigenvalues are obtained by diagonalizing H_{lm} . In general the matrix H_{lm} is infinitely large. However, due to the fact that $H_{lm} = 0$ for $|l - m| \neq 0$ or 1, and because we are only interested in the lowest bands (i.e. the first few eigenvalues), the matrix can be truncated and diagonalized.

In Fig. 3.7 the first four energy eigenvalues are plotted versus quasi-momentum q . For the calculation of the eigenvalues a 6×6 matrix is used, i.e. H_{lm} is truncated for $l, m > 6$. The ‘‘band structure’’ plots show, that for non-zero potential depths the particle’s energy

can not have arbitrary values. Every allowed energy range is called an *energy band* and is determined by one of the eigenvalues $E_{n,q}$. The forbidden region in between two bands is named the *band gap* and becomes larger for increasing lattice depth.

The state of an atom, initially in state $\phi_{n,q}(z)$, develops as

$$\begin{aligned}\psi(z, t) &= e^{-itE_{n,q}/\hbar} \phi_{n,q}(z) \\ &= e^{-itE_{n,q}/\hbar} e^{iqz/\hbar} u_{n,q}(z)\end{aligned}\quad (3.33)$$

3.3.2. Accelerated lattice - Bloch oscillations

If the frequencies of the two lattice beams do not exactly coincide, the lattice will move. Assuming two beams with the same amplitude E_0 , the resulting field is

$$\begin{aligned}E &= E_0 [\cos(k_1 z + \omega_1 t) + \cos(-k_2 z + \omega_2 t)] \\ &= 2E_0 \cdot \cos\left(kz - \frac{\Delta\omega}{2}t\right) \cdot \cos\left(\omega t - \frac{\Delta k}{2}z\right)\end{aligned}\quad (3.34)$$

where $k_{1,2} = k \mp \Delta k/2$ are the wavevectors and $\omega_{1,2} = \omega \mp \Delta\omega/2$ the frequencies of the two beams. From the second term we learn, that the oscillation frequency of the field slightly deviates from ω depending on the axial position z . The first term on the other hand shows, that the resulting field may be seen as a standing wave with wave vector $k = \frac{k_1+k_2}{2}$, which is moving at a velocity

$$v_{\text{lattice}} = \frac{\Delta\omega}{2k}\quad (3.35)$$

Again, we want to restrict the treatment to a linear frequency sweep of one beam relative to the other one

$$\Delta\omega(t) = \omega_1 - \omega_2(t) = \dot{\omega}_2 t\quad (3.36)$$

with $\dot{\omega}_2 = \text{const.}$, corresponding to a linearly accelerated lattice. The dynamics of a particle in such a linearly accelerated lattice potential may also be described by a Hamiltonian of the following form [Pei97]

$$H = \frac{p^2}{2m} - U_{\text{latt}} \cos^2 kx - Fx\quad (3.37)$$

where the constant force F is given by

$$F = m\dot{v}_{\text{lattice}} = m\frac{\dot{\omega}_2}{2k}\quad (3.38)$$

The Bloch waves are no longer eigenfunctions of the system. However, when F is weak enough to not induce band transitions, they may still be used to derive the time evolution of the wave function [Pei97]

$$\psi(x, t) = e^{-i\int_0^t d\tau E_n(q(\tau))/\hbar} e^{iq(t)x/\hbar} u_{n,q(t)}(x)\quad (3.39)$$

This is the same time evolution as for the non-moving lattice, except that the stationary quasimomentum q is now substituted by

$$q(t) = q_0 + Ft. \quad (3.40)$$

In the Bloch band picture this means, that the atoms are swept through momentum space due to the external force F . The time it takes to scan through one full Brillouin zone $-\hbar k \leq q \leq \hbar k$ is given by the Bloch period

$$\tau_B = \frac{2\hbar k}{|F|} \quad (3.41)$$

The expression for the Bloch period $t_B = 8\omega_r/\dot{\omega}_2$ used in the caption of Fig. 3.5 is then obtained by plugging (3.38) into (3.41).

When the band structure is known, the mean velocity of the particle in the lattice frame may be derived [Kit87]

$$\bar{v}'_n(q) = \frac{dE_n(q)}{dq} \quad (3.42)$$

In Fig. 3.8 the calculated values for $\bar{v}'_n(q)$ are compared to the data already shown in Fig. 3.6 but with the lattice velocity subtracted. Furthermore (3.42) may be plugged into (3.24) in order to get an expression for the mean velocity in the laboratory frame $\bar{v}(t)$. The results coincide with the one from the previous section. Thus both approaches predict indeed the same kinetic behavior for atomic clouds, exposed to an accelerated lattice potential.

Moreover (3.42) shows, that not only $E_n(q)$, but also $\bar{v}'_n(q)$ is a periodic function of q - and consequently also periodic in t . The period of these ‘‘Bloch oscillations’’ (BO) is given by τ_B (Fig. 3.8). In the 1930’s Bloch and Zener already predicted, that electrons in solids under the influence of an external electric field should exhibit these BO. However scattering at lattice defects makes it impossible to observe these oscillations in solids. An exception are the so-called superlattices. In these artificial lattices with very large periodicities, the Bloch period is smaller than the typical time between two scattering processes and the BO become visible [Was93].

For the derivation of $\bar{v}'(t)$ we have made the assumption, that the force $F = m\dot{v}_{\text{latt}}$ is weak enough to not induce transitions into higher bands. It was shown by Zener [Zen32], that in order to keep the probability for tunneling into higher bands much smaller than 1, the acceleration F has to be

$$F \ll m \frac{\pi U_0^2}{16\hbar^2 k}. \quad (3.43)$$

By setting $F = m\dot{v}_{\text{latt}} = m\dot{\omega}_2\lambda/(4\pi)$ one can see, that this is exactly the same adiabaticity criteria as the one obtained with the ARP model of the previous section (equation (3.18)).

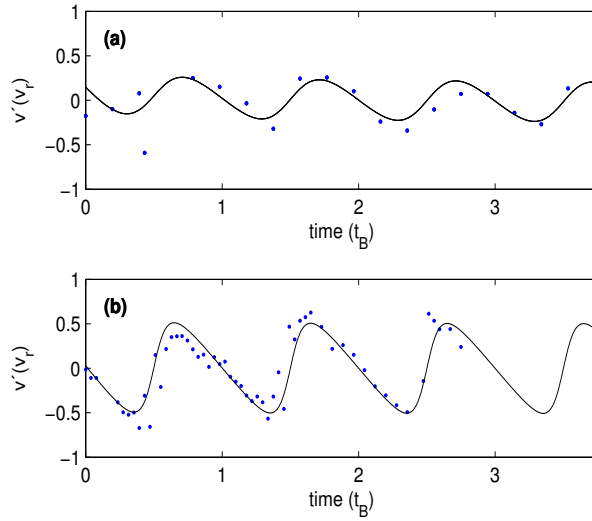


Figure 3.8.: Bloch oscillations: The mean velocity of the atomic sample in the reference frame of the linearly accelerated lattice as a function of time t for **(a)** $U_0 = 4.4E_r$ and **(b)** $U_0 = 1.8E_r$. The time is given in units of the Bloch period t_B . For the deeper lattice shown in figure **(a)**, the oscillations are less pronounced.

3.3.3. Atomic interactions and instabilities

So far we have discussed non-interacting atomic clouds in optical lattices. In this subsection we want to add another term to the Hamiltonian, describing the interaction between the atoms. For a Bose-condensed samples at ultra-low temperatures the total Hamiltonian may be written as

$$H = \frac{p^2}{2m} - U_0 \cos^2 kx + \frac{4\pi\hbar^2 a_s}{m} |\psi(x, t)|^2 \quad (3.44)$$

where the interactions are described by a single parameter, namely the s-wave scattering length a_s . The corresponding Schrödinger equation is *non-linear*, since the Hamiltonian itself contains the square of the total wavefunction $\psi(x, t)$. Because of its great importance in the field of Bose-Einstein condensates [Pet02], this equation got its own name; it is called the Gross-Pitaevskii equation (GPE).

Landau and dynamical instabilities

Instabilities in superfluid systems, such as BECs, is a wide field of research. However, since our main focus is not to study those instabilities, but to avoid them, we devote only a short discussion to them.

A thorough stability analysis of the GPE with the Hamiltonian (3.44) shows, that BECs with attractive *as well as with repulsive* interactions ($a_s > 0$) may be unstable in the presence of a periodic potential [Cho99, Wu03, Fal04, Cri04].

In general Landau instability occurs, when the overall energy of a superfluid system may be lowered by the creation of phonons. In free space a superfluid is described by a plane wave, for which this unstable point is reached, when the speed of the superfluid reaches the speed of sound. In a periodic potential a BEC may be described by Bloch waves, for which Landau instability typically occurs near the edge of the Brillouin zone.

Dynamical instabilities exist in free space only for BECs with attractive interactions. However, in the presence of an external lattice potential, the effective mass of the condensate may become negative close to the edge of the Brillouin zone. As a consequence repulsive interactions turn attractive in this region of the momentum space and the BEC can decay. For an exact determination of the unstable region, the lattice depth as well as the interactions energy have to be known.

In our transport experiments we typically have lattice depths on the order of $10 E_r$ and interaction energies of approximately $4\pi\hbar^2 a_s n/m \approx 1 E_r$ for a background scattering length $a_s = 100 a_{\text{Bohr}}$ and a density of $n \approx 7 \times 10^{13} \text{ cm}^{-3}$. In this case about half of the Brillouin zone ($k/2 \leq |q| < k$) is unstable with respect to both Landau and dynamical instabilities. The lifetime of a BEC is strongly reduced in this region and is only on the order of 10 ms [Fal04]. In our experiment we observe, that by sweeping through the Brillouin zone in much less than $\Delta t = 20 \text{ ms}$, the instabilities are suppressed. This value for Δt corresponds to the following constraint for the acceleration: $a = \dot{v} \gg 2v_r/\Delta t \simeq 0.6 \text{ m/s}^2$. By keeping the acceleration above this value, we find, that BECs may be transported without losing coherence and introducing too much heating through these instabilities. In general it would be interesting to understand further this kind of self-healing mechanism, that leads to the suppression of the instabilities. However, within the framework of this thesis, there was not enough time to further investigate the physics of these instabilities.

4. Experiments with moving lattices

In the first part of this chapter a short explanation of how to create a Bose-Einstein condensate and how to load it into a standing wave is provided. Afterwards the main focus is set on the transport experiments. In various measurements the long distance transport of ultracold atoms is studied. Eventually it is shown, how the idea of an atom catapult may be realized.

4.1. Experimental setup

4.1.1. Making a Bose-Einstein Condensate

Ten years after the first observation of Bose-Einstein Condensation (BEC) in dilute atomic clouds [And95, Dav95], numerous BEC setups exist worldwide. All the experiments rely on laser cooling and trapping techniques [Met99] as well as on evaporative cooling, which were all developed over the last few decades.

In our experiment (Fig. 4.2) the cycle starts with capturing about 5×10^9 atoms from a background Rubidium (^{87}Rb) vapor in a magneto-optical trap (MOT) (for a more detailed description of the BEC setup see [The05]). After a short molasses cooling stage the sample is spin-polarized into the $|F = 1, m_F = -1\rangle$ state. The atoms are then loaded into a magnetic quadrupole trap, formed by the quadrupole coils of the MOT. By using a magnetic conveyor belt [Gre01] the cloud is then pushed from the MOT chamber over approximately 40 cm into the glass cell, located at the end of the XUHV region. Once arrived in the glass cell, the atoms are loaded into a QUIC trap [Ess98] with trap frequencies of (15Hz, 150Hz, 150Hz). In this magnetic trap evaporative cooling with

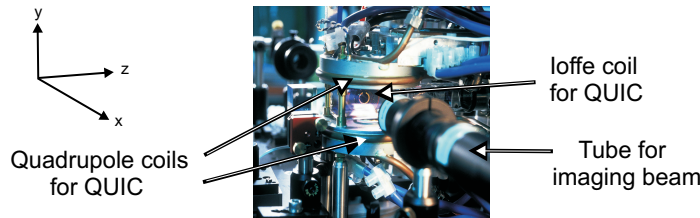


Figure 4.1.: PICTURE OF THE GLASS CELL: The BEC is produced in the glass cell, which is surrounded by the coils for the QUIC-trap. From this point of view, the so-called Ioffe coil is located behind the cell. It is needed to generate a magnetic field with a non-zero minimum, as required for BEC-trapping. The imaging beam for the main camera points along the x -direction, so that high quality (y, z) -profiles of the condensate are obtained.

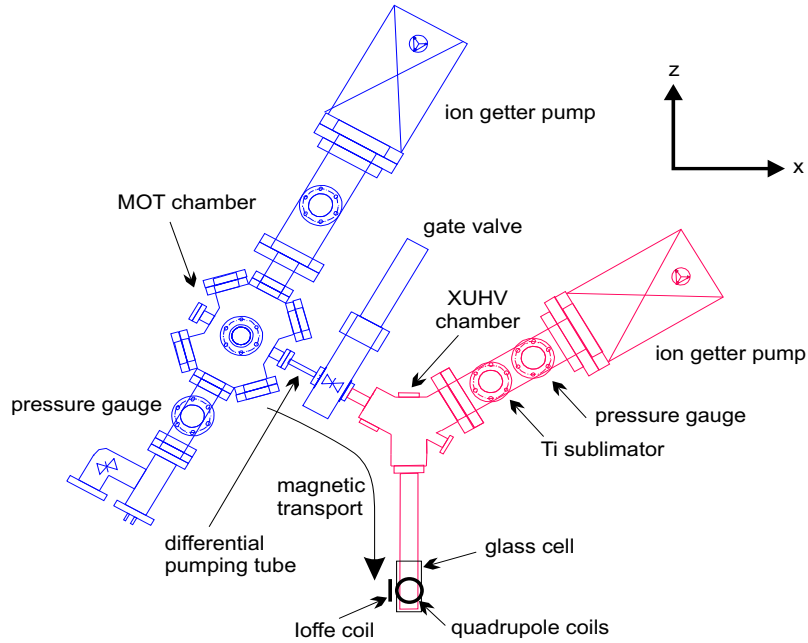


Figure 4.2.: BEC APPARATUS: Magnetic field are used to transport the atoms from the MOT section (left) to the XUV section (right) and eventually into the glass cell, where the BEC is produced.

initially about 5×10^8 atoms is launched. Eventually all remaining 5×10^5 atoms are Bose condensed, resulting in a purely parabolic velocity distribution. Since the center of the QUIC trap and therefore the BEC is located very close to the wall of the cell, the currents through the QUIC- and the offset-coils are readjusted after evaporation. The resulting trap is now a fairly shallow “Ioffe-type” trap with trap frequencies of (7Hz, 19Hz, 20Hz). Along the x -direction this trap is now centered with respect to the glass cell. Therefore the two required laser beams (propagating along the z -direction), which have to be overlapped with the BEC, can now conveniently be guided through the center of the glass cell. (Fig. 4.3). This way the beams will less likely hit the corners of the glass cell and therefore unwanted aperture effects are avoided.

4.1.2. Loading the standing wave trap

From the magnetic trap the condensate is loaded into a 1D optical lattice formed by a Bessel beam of radius $r_0 = 36\mu\text{m}$ and a counterpropagating Gaussian beam with a waist of $w_0 \approx 85\mu\text{m}$ (Fig. 4.3 and Fig. 4.4). This rather small value for the waist of the Gaussian beam was chosen, because the corresponding beam was readily available and the time to set up the beams was very limited. However, in principle a larger waist and thus a larger Rayleigh range would of course be advantageous. The power needed for the Bessel beam to support the atoms against gravity is typically 200mW, since only a few percent ($\approx 10\text{mW}$) of the total power are stored in the central spot. For the Gaussian

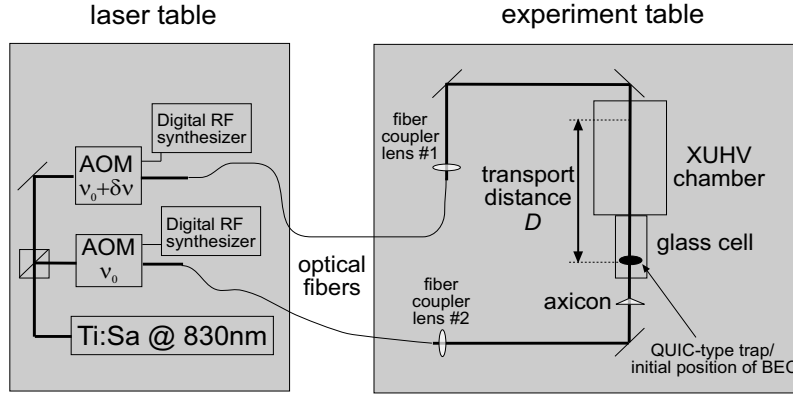


Figure 4.3.: SETUP FOR THE TRANSPORT: The light for the 1D lattice is obtained from a Ti:Sapph-laser operated at a wavelength of 830 nm. The two beams are both sent through acousto-optical modulators to introduce the required detuning. Then they are sent from the laser table to the experiment table via 10 m long, single mode & polarization maintaining fibers. The aspheric lens of the fiber coupler #1 is used to generate a Gaussian beam with a focus located approximately between the XUV chamber and the glass cell. Fiber coupler lens #2 is used to generate a collimated beam with waist $w_0 = 1$ mm and 2 mm, respectively. The axicon is placed about 2 cm in front of the glass cell.

beam a power of roughly 20mW is chosen, leading to a trapping potential at the center ($r = 0$) of $U(z) = -U_0 + U_{latt} \cos^2(kz)$, where the lattice depth (effective axial trap depth) is $U_{latt} \approx 10E_r$ and the total trap depth $U_0 \approx 11E_r$. The corresponding trap frequencies are

$$\begin{aligned} \nu_{\perp} &= \frac{4.81}{2\pi} \sqrt{\frac{U_0}{8mr_0^2}} = 97\text{Hz} \\ \nu_z &= \frac{k}{2\pi} \sqrt{\frac{2U_{latt}}{m}} = 21\text{kHz}. \end{aligned} \quad (4.1)$$

The first main task of the experiment is to load the BEC from the magnetic trap into the standing wave without exciting it. In the presence of the lattice, the energy eigenvalues and eigenfunctions of the system are given by the Bloch eigenenergies $E_{n,q}$ and -functions $|\phi_{n,q}\rangle$, which are defined through equation (3.26). The goal is to keep the atoms in the lowest band $n = 0$. To not populate any bands with $n' > 0$, the adiabaticity criterion [Sch68] has to be fulfilled

$$|\langle \phi_{n=0,q} | \frac{dH}{dt} | \phi_{n'>0,q} \rangle| \ll \frac{|E_{n=0,q} - E_{n'>0,q}|^2}{\hbar}. \quad (4.2)$$

Since the lattice is at rest during loading ($q = 0$) we may write for the term on the right hand side $|E_{n=0,q=0} - E_{n'>0,q=0}| \geq 4E_r$, where the equal sign is for vanishing lattice

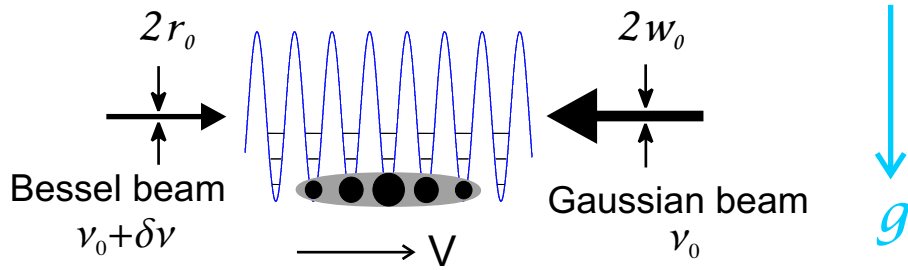


Figure 4.4.: SETUP FOR TRANSPORT EXPERIMENTS: Two counterpropagating beams (a Gaussian beam with diameter $2w_0$ and a Bessel beam with diameter $2r_0$) are forming a standing wave trap. The atoms are loaded adiabatically into the nodes of this standing wave. In fact the number of occupied nodes is on the order of 100. By detuning one of the beams by $\Delta\nu = \Delta\omega/(2\pi)$ the standing wave starts to move at a velocity $v = \Delta\omega/(2k)$, where $k = 2\pi/\lambda$.

depth (see also the Band structure shown in Fig. 3.7). Thus the amplitude is ramped such that

$$\frac{\dot{V}_0}{E_r} \ll 16 \frac{E_r}{\hbar} \quad (4.3)$$

In our case (^{87}Rb in a 830nm standing wave) the recoil energy is $E_r = \hbar/(2\pi) \times 3.3 \text{ kHz}$, which leads to a value for the right hand side of (4.3) of $16 \frac{E_r}{\hbar} \simeq 2 \times 10^5 \text{ s}^{-1}$. This means, one should take up significantly more than $50\mu\text{s}$ to increase the lattice depths by one recoil; i.e. to load a $10E_r$ lattice 5ms should be a fair choice for the ramp time.

When (4.2) is fulfilled, the loading is adiabatic with respect to the single particle states. However, to be adiabatic with respect to an entire cloud of interacting atoms, one has to ensure, that the chemical potential of the ensemble stays uniform at any instant of time [Bla04]. In our case of a lattice potential the time needed to compensate for imbalances in the chemical potential is given by the tunneling time. Thus we choose a ramp time much larger than the typical tunneling time.

For our lattice parameters the tunneling time is on the order of 10ms. As expected from the consideration above, we observe, that the ramp time needs to be on the order of 100ms or larger. Eventually 100 ms and 130 ms, respectively, was chosen for basically all experiments presented here.

For the shape of the amplitude ramp $A(t)$, which determines the lattice depth during the loading process, we pick a polynomial function of third order. With the four constraints $A(0) = A'(0) = A'(T) = 0$ and $A(T) = 1$ the coefficients are well-defined and a smooth ramp of the following form is obtained.

$$A(t) = -2 \left(\frac{t}{T} \right)^3 + 3 \left(\frac{t}{T} \right)^2 \quad (4.4)$$

where $T = 100\text{ms}$ is the ramp time. An analogous function is used to ramp down the amplitude.

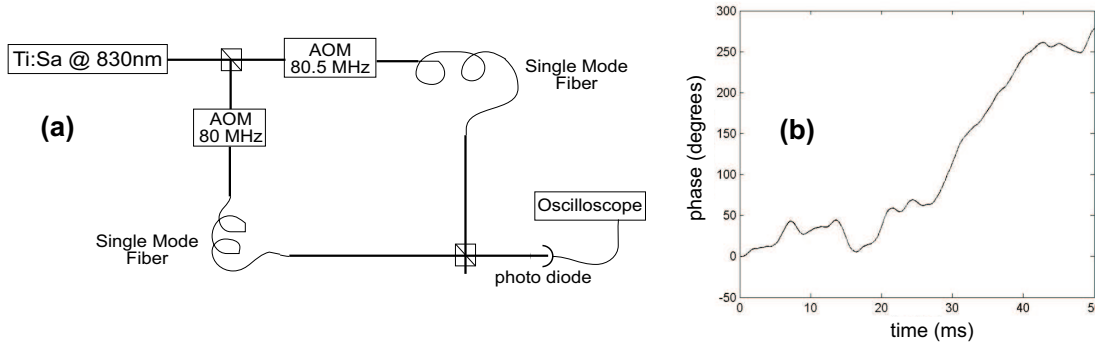


Figure 4.5.: (a) Test setup for the phase stability measurement: The light at a wavelength of 830 nm is split into two beams. Then both beams are passed through acousto-optical modulators (AOMs) operated at slightly different frequencies of 80 MHz and 80.5 MHz. The synthesizers generating those radio-frequency signals are phase-locked, as discussed. After being sent through 10 m long, single mode optical fibers, the two beams are overlapped again and the beat between them at a frequency of 500 kHz can be detected using a photo diode. (b) Phase drift of the beat signal: The phase of the beat is compared to the phase of an ideal sine wave and then plotted as a function of time. A drift on the order of 360° is observed.

4.1.3. Setup for acceleration - creating a phase stable moving standing wave

As mentioned in the previous chapter the two counterpropagating beams have to be slightly detuned from each other in order to obtain a moving lattice. In the actual experiment this detuning $\Delta\omega$ is introduced by passing both beams through acousto-optical modulators (AOMs). The radio frequency (RF) for the first AOM is kept constant at $\omega_1/(2\pi) = 80$ MHz, where as the second one is swept appropriately $\omega_2(t) = \omega_1 + \Delta\omega(t)$. Both RF signals are generated by digital synthesizers (AD9854), with which we have full control over amplitude, frequency and phase at any instant of time. Therefore these programmable RF-sources do not only provide the frequency but also the amplitude ramp for loading and unloading. For more details about these digital synthesizers the reader is referred to appendix A. A very important feature of the AD9854 is the possibility to lock it to an external reference oscillator. This enables us to phase lock the radiowave signals for the two AOMs.

However, even when the lattice beams are phase locked right after passing the AOM, their phase may have drifted once they reach the BEC in the glass cell. In particular the 10 m long optical fiber (Fig. 4.3) between the laser table and the experiment table can be a source for phase and polarization drifts. For this reason, in advance to the transport experiments the phase drift was estimated with a measurement of the relative phase between the two fiber-coupled beams.

The beat between the two beams at a frequency of 500 kHz is detected as described in

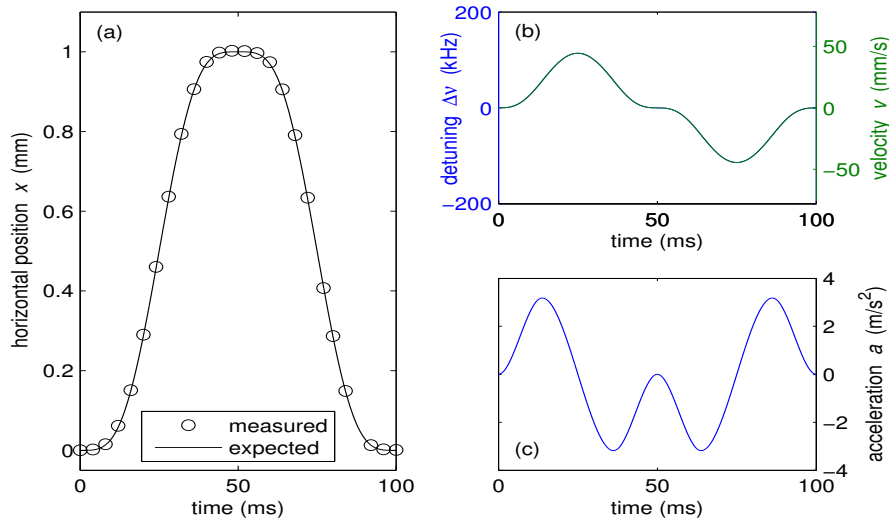


Figure 4.6.: (a) Position, (b) velocity and (c) acceleration of the atomic cloud as a function of time for a typical transport sequence, here a round-trip over a short distance of 1mm. Piecewise defined cubic polynomials are used for the acceleration ramp. By integrating over time, velocity, position and frequency detuning -used to program the synthesizers- are derived. The position ramp is compared with in-situ measurements of the cloud’s position (circles)

Fig. 4.5(a) and stored using an oscilloscope. The phase of this beat signal is compared to the phase of an ideal sine wave $\varphi_{\text{sine}}(t) = 2\pi \times 500 \text{ kHz} \times t$. On the time scale of 50 ms, which is only about a factor of 4 or 5 less than the time scale of our experiments, phase drifts on the order of 360° are observed (Fig. 4.5(b)). This phase drift corresponds to a position drift on the order of the laser wavelength. As we will see later, this is in good agreement with the position uncertainty, observed in the transport experiments. The main reasons for the slow phase drifts are polarization and temperature drifts within the optical fibers.

4.2. Transport experiments

4.2.1. Basic Transport Kinematics

For the acceleration a piecewise defined cubic polynomial (“cubic spline”) is chosen

$$a(t) = \begin{cases} \frac{D}{T^2} \left(-\frac{7040}{9} \left(\frac{t}{T}\right)^3 + 320 \left(\frac{t}{T}\right)^2 \right) & \text{for } 0 < t \leq T/4 \\ \frac{D}{T^2} \left(\frac{3200}{9} \left(\frac{t}{T}\right)^3 - \frac{1600}{3} \left(\frac{t}{T}\right)^2 + \frac{640}{3} \frac{t}{T} - \frac{160}{9} \right) & \text{for } T/4 < t \leq 3T/4 \\ \frac{D}{T^2} \left(-\frac{7040}{9} \left(\frac{t}{T}\right)^3 + \frac{6080}{3} \left(\frac{t}{T}\right)^2 - \frac{5120}{3} \frac{t}{T} + \frac{4160}{9} \right) & \text{for } 3T/4 < t \leq T \\ \text{for} & \end{cases} \quad (4.5)$$

where D is the covered distance and T the duration. By making this choice $a(t)$ and its derivative $\dot{a}(t)$ are zero at the beginning $t = 0$ and at the end $t = T$ of the transport. For $t = 1/4$ and $T = 3/4$ the acceleration reaches a maximum.

Given the expression for $a(t)$ the velocity $v(t)$ and the position $x(t)$ may be calculated by integration over time.

$$v(t) = \begin{cases} \frac{D}{T} \left(-\frac{1760}{9} \left(\frac{t}{T}\right)^4 + \frac{320}{3} \left(\frac{t}{T}\right)^3 \right) & \text{for } 0 < t \leq T/4 \\ \frac{D}{T} \left(\frac{800}{9} \left(\frac{t}{T}\right)^4 - \frac{1600}{9} \left(\frac{t}{T}\right)^3 + \frac{320}{3} \left(\frac{t}{T}\right)^2 - \frac{160}{9} \left(\frac{t}{T}\right) + \frac{10}{9} \right) & \text{for } T/4 < t \leq 3T/4 \\ D \left(-\frac{1760}{9} \left(\frac{t}{T}\right)^4 + \frac{6080}{9} \left(\frac{t}{T}\right)^3 - \frac{2560}{3} \left(\frac{t}{T}\right)^2 + \frac{4160}{9} \left(\frac{t}{T}\right) - \frac{800}{9} \right) & \text{for } 3T/4 < t \leq T \end{cases}$$

$$x(t) = \begin{cases} D \left(-\frac{352}{9} \left(\frac{t}{T}\right)^5 + \frac{80}{3} \left(\frac{t}{T}\right)^4 \right) & \text{for } 0 < t \leq T/4 \\ D \left(\frac{160}{9} \left(\frac{t}{T}\right)^5 - \frac{400}{9} \left(\frac{t}{T}\right)^4 + \frac{320}{9} \left(\frac{t}{T}\right)^3 - \frac{80}{9} \left(\frac{t}{T}\right)^2 + \frac{10}{9} \frac{t}{T} - \frac{1}{18} \right) & \text{for } T/4 < t \leq 3T/4 \\ D \left(-\frac{352}{9} \left(\frac{t}{T}\right)^5 + \frac{1520}{9} \left(\frac{t}{T}\right)^4 - \frac{2560}{9} \left(\frac{t}{T}\right)^3 + \frac{2080}{9} \left(\frac{t}{T}\right)^2 - \frac{800}{9} \frac{t}{T} + \frac{121}{9} \right) & \text{for } 3T/4 < t \leq T \end{cases} \quad (4.6)$$

The velocity ramp $v(t)$ is then plugged into equation (3.35), in order to obtain the appropriate frequency ramp for the synthesizers.

Figure 4.6 shows results of a first experiment, where we have transported atoms over short distances of 1 mm (round trip 2 mm). The atoms move perpendicularly to the direction of observation and never leave the field of view of the CCD camera. In-situ images of the atomic cloud in the optical lattice were taken at various times during transport, and the center of mass position of the cloud was determined. By comparing the theoretically expected position given by equation (4.6) with the position, obtained from the in-situ images, we verify, that we have full control over the kinematic quantities (Fig. 4.6(a)).

4.2.2. Transport of ultracold atoms using a Gaussian beam lattice

Even though the data shown in Fig. 4.6(a) were obtained for a Bessel-Gauss lattice, transport over small distances may also be realized using two counterpropagating Gaussian beams. For this purpose we have performed measurements with Gaussian beams, both having a Rayleigh range of $z_R \approx 2$ cm corresponding to a waist of $70 \mu\text{m}$. The laser power of the two beams was ≈ 130 mW and ≈ 35 mW, respectively. We observe a sudden drop in atom number when the transport distance exceeds the Rayleigh range (Fig. 4.7). This is in agreement with the expectations, since for the beam parameters given above, the atoms are only held against gravity at axial positions $z < z_R$. In the following we want to show, why the transport of atoms over tens of cm using a Gaussian lattice is hard to achieve.

As an example, we assume, that we want to transport over a distance of 50 cm. During transport we require the maximum radial confining force F_{max} to be larger than gravity mg , where m is the atomic mass and $g \approx 9.81 \text{ m/s}^2$ is the acceleration due to gravity. For a Gaussian beam this is

$$F_{\text{max}} = \frac{3}{4\pi^3 \sqrt{e}} \frac{\lambda^3}{c} \frac{\Gamma}{\Delta} \frac{P_0}{w(z)^3} > mg \quad (4.7)$$

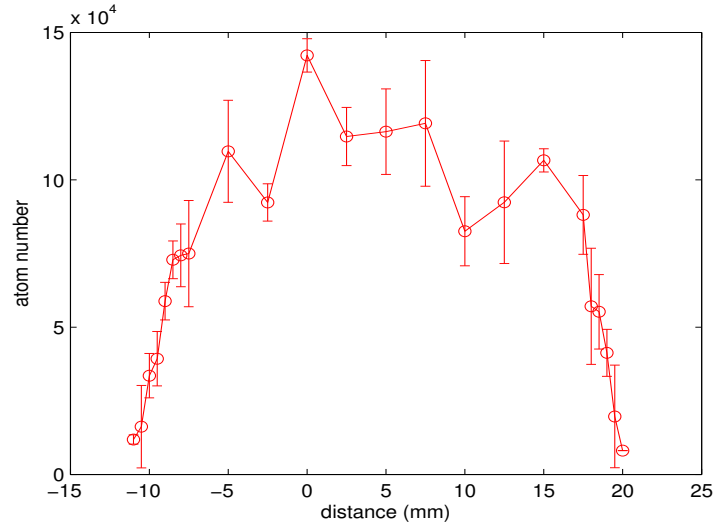


Figure 4.7.: TRANSPORT IN A GAUSSIAN BEAM LATTICE: The atom number is plotted versus transport distance. We estimate, that for distances exceeding 20 mm in the one direction and 10 mm in the other direction, respectively, the atoms are not hold against gravity any more and get lost.

where Γ is the natural linewidth of the relevant atomic transition, Δ the detuning from this transition, $w(z)$ the beam radius and P_0 the total power of the beam. The strong dependence on the beam radius $w(z)$ suggests, that $w(z) = w_0\sqrt{1 + (z/z_R)^2}$ should not vary too much over the transport distance. If we thus require the Rayleigh range $z_R = \pi w_0^2/\lambda$ to equal the distance of 25 cm, the waist has to be $w_0 \approx 260 \mu\text{m}$. For a lattice beam wavelength of e.g. 830 nm, the detuning from the D-lines of ^{87}Rb is $\Delta \approx 2\pi \times 130 \text{ THz}$. To hold the atoms against gravity for all z , where $|z| < z_R$, a total laser power of $P_0 \approx 10 \text{ W}$ is needed, which is difficult to produce. In addition the spontaneous photon scattering rate

$$\Gamma_{\text{scatt}} = \frac{3}{8\pi^3\hbar} \frac{\lambda^3}{c} \left(\frac{\Gamma}{\Delta}\right)^2 \frac{P_0}{w(z)^2} \quad (4.8)$$

would reach values on the order of $\Gamma_{\text{scatt}} = 2 \text{ s}^{-1}$. For typical transport times of 200 ms this would mean substantial heating and atomic losses.

4.2.3. Transport of ultracold atoms using a Bessel-Gauss lattice

A better choice for transport are zero order Bessel beams. In our experiments we have formed a standing light wave by interfering a Bessel beam with a counter-propagating Gaussian beam, giving rise to an optical lattice which is radially modulated according to the Bessel beam (see equations (2.35) to (2.37)). Atoms loaded into the tightly confined inner spot of the Bessel beam can be held against gravity for moderate light intensities, which minimizes the spontaneous photon scattering rate. In contrast to the transport

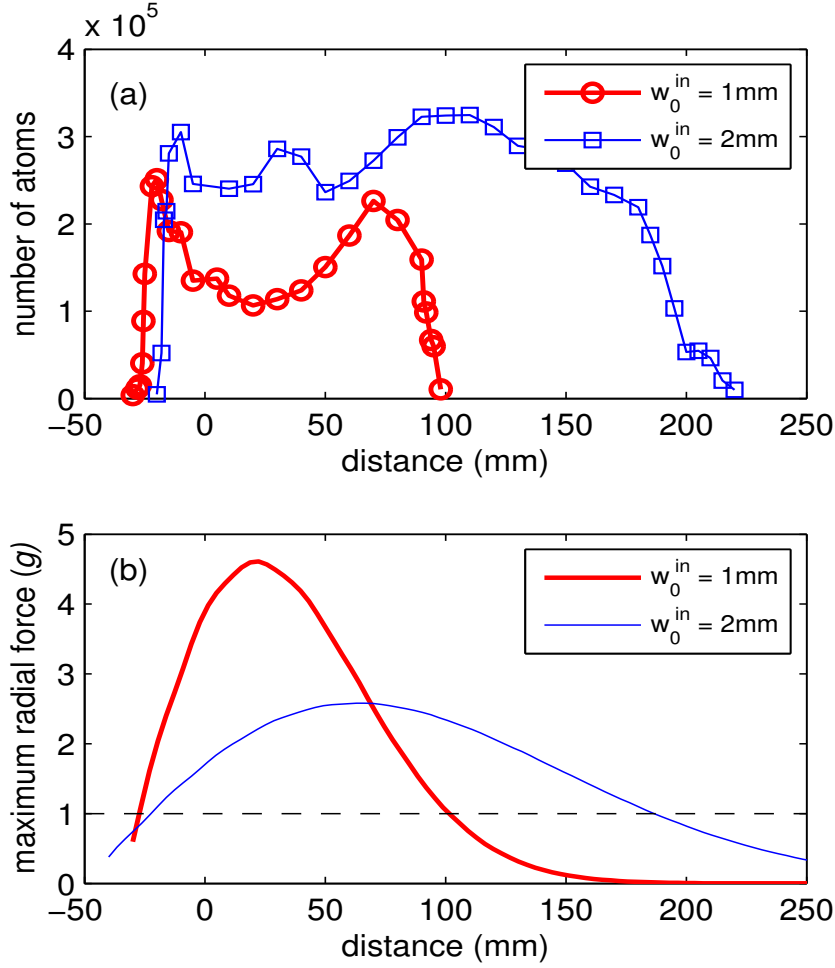


Figure 4.8.: LONG DISTANCE TRANSPORTS. (a) Shown is the number of remaining atoms after a round-trip transport (see Fig. 4.6) over various (one way) distances. The two data sets are obtained with two different Bessel beams which are created by illuminating an axicon with a Gaussian beam with a waist $w_0^{\text{in}} = 1\text{ mm}$ and 2 mm , respectively. The transport time was kept constant at $T = 130\text{ ms}$ and $T = 280\text{ ms}$. The calculated maximum radial trapping force of these two Besselbeams is shown in (b) in units of mg , where $g \approx 9.81\text{ m/s}^2$ denotes the gravitational acceleration. The variation of the trapping force with distance is an imperfection of the Bessel beam and reflects its creation from a Gaussian beam. When the maximum radial force drops to below 1 g , gravity pulls the atoms out of the trap, as can be clearly seen in (a).

with a Gaussian beam, the scattering rate in a Bessel beam transport can be kept as low as 0.05 s^{-1} by using the beam parameters of our experiment.

With such a lattice the transport scheme presented in Fig. 4.6 can readily be extended to distances of up to 1 m. The distance is limited to this value, due to the finite range of the Bessel beam (Fig. 4.8(b)). The range, for which the radially confining force is larger than gravity, depends on the power available. In our case the maximally available power was approximately 400 mW, with which we were able to reach distances of 20 cm (40 cm round-trip). As shown in Fig. 4.8, the total number of atoms abruptly decreases at the axial position, where the maximum radial force drops below gravity. It is also clear from the figure, how the range of the Bessel beam is increased by enlarging the waist w_0^{in} of the Gaussian laser beam at the location of the axicon. Of course, for a given total laser power, the maximum radial force decreases as the Bessel beam diameter is increased. For both transports over 12 cm and 20 cm the total power in the Bessel beam was approximately 400 mW.

Interestingly, the curve corresponding to the Bessel beam with waist $w_0^{\text{in}} = 1 \text{ mm}$ in Figure 4.8(a) exhibits a pronounced minimum in the number of remaining atoms at a distance of about 3 cm. The position of this minimum coincides with the position, where the lattice depth has a maximum (see Figure 4.8(b)). This clearly indicates, that high light intensities adversely affect atom lifetimes in the lattice. Although we have not studied in detail the origin of the atomic losses in this work, they should partially originate from spontaneous photon scattering and 3-body recombination. In the deep lattice here ($60 E_T$) the calculated photon scattering rate is $\Gamma_{\text{scatt}} = 0.4 \text{ s}^{-1}$. The tight lattice confinement leads to a high calculated atomic density of $n_0 \approx 2 \cdot 10^{14} \text{ cm}^{-3}$. Adopting $L = 5.8 \times 10^{-30} \text{ cm}^6/\text{s}$ as rate coefficient for the three body recombination [S99], we expect a corresponding loss rate $Ln_0^2 = 0.3 \text{ s}^{-1}$.

4.2.4. Transport of a BEC over macroscopic distances

In Fig. 4.9 and Fig. 4.10 we have studied the transport of a BEC, which is especially sensitive to heating and instabilities. The question is to which extent are the atoms still Bose-condensed after the transport and what is their temperature afterwards? Figure 4.9 shows time-of-flight pictures for various transport distances D , which were obtained after adiabatic switch-off of the lattice and abrupt switch-off of the magnetic trap. Additionally a more quantitative analysis of the momentum distribution is provided in Fig. 4.10.

Before discussing these results, we point out that loading the BEC adiabatically into the stationary optical lattice and subsequent holding is already critical. We observe a strong dependence of the condensate fraction on the lattice depth (Fig. 4.11). For too low lattice depths most atoms fall out of the lattice trap due to the gravitational field. For too high lattice depths all atoms are trapped but the condensate fraction is very small. One explanation for this is that high lattice depths lead to the regime of 2D pancake shaped condensates where tunnelling between adjacent lattice sites is suppressed. Relative dephasing of the pancake shaped condensates will then reduce the condensate fraction after release from the lattice. We obtain the best loading results

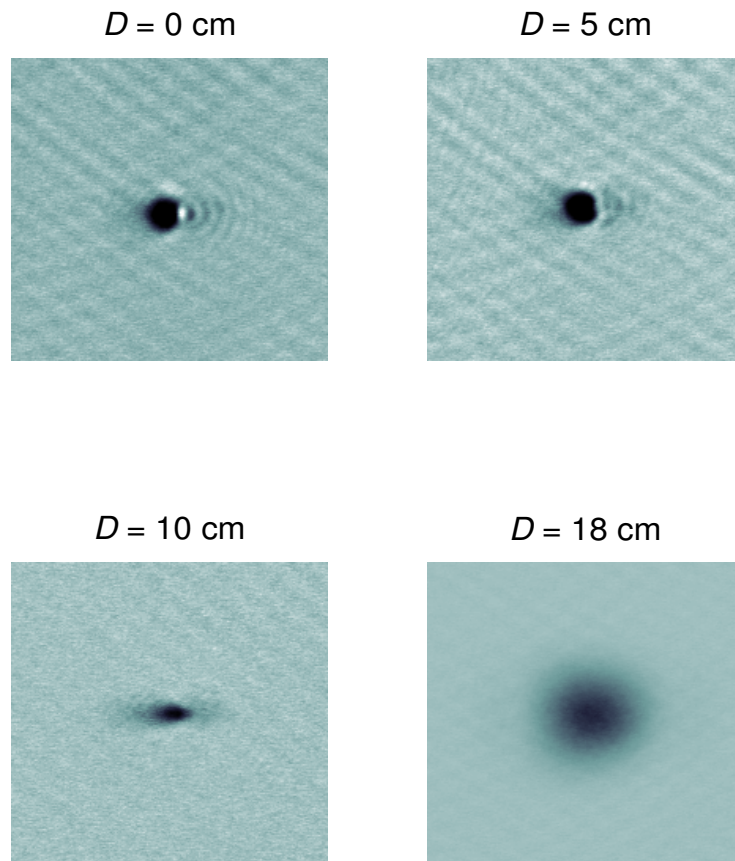


Figure 4.9.: TIME-OF-FLIGHT PICTURES OF THE CLOUD: After transport the atoms are adiabatically reloaded into the magnetic trap. From there they are released abruptly and images are taken after 12 ms time-of-flight. This way the momentum distribution of the atoms is measured. For small one-way transport distances on the order of $D = 5$ cm the majority of the atoms is still Bose-condensed (see also Fig. 4.10). However, an increasing momentum spread is observed for larger transport distances. For 18 cm the sample was fully thermal. The diffraction rings seen in the upper figures are due to an imaging problem.

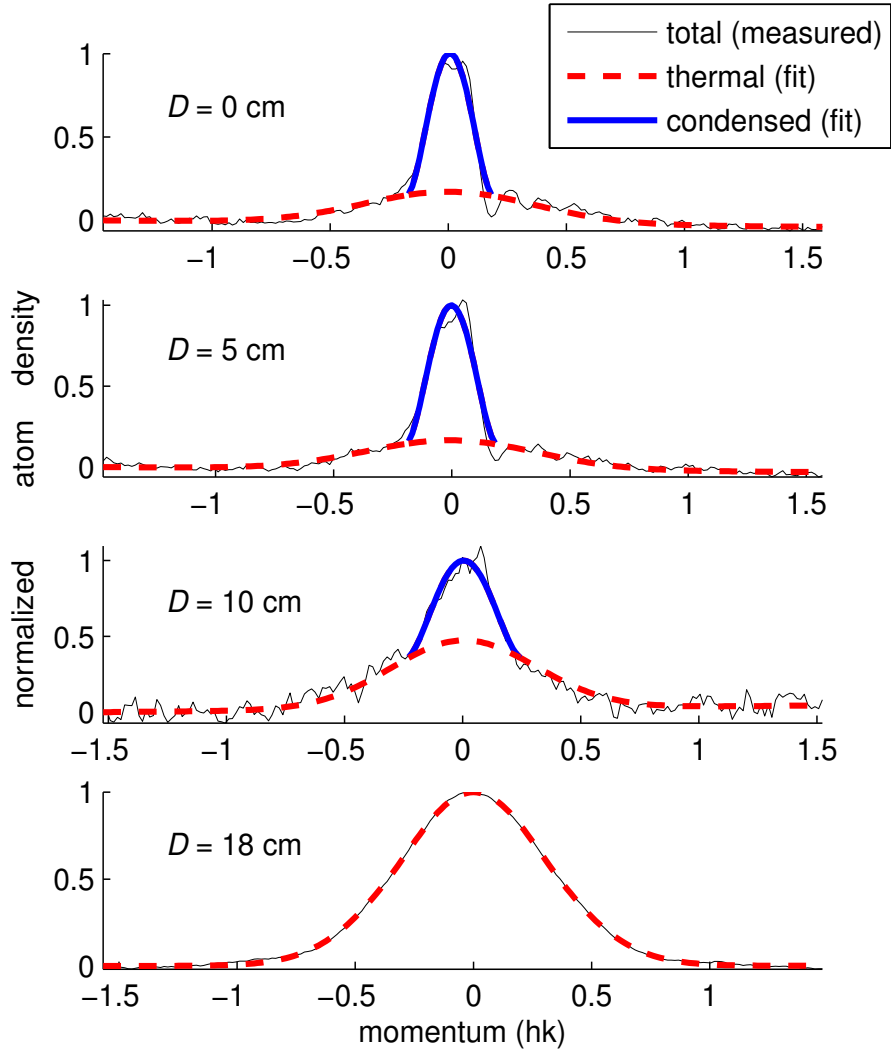


Figure 4.10.: TRANSPORTING BEC. Shown are the momentum distributions (thin black lines) of the atoms after a return-trip transport over various one-way distances D . A bimodal distribution (a blue parabolic distribution for the condensed fraction and a red Gaussian distribution for the thermal fraction) is fit to the data. For D below 10cm a significant fraction of the atomic cloud is still condensed. For $D = 18$ cm (\approx the limit in our experiments) only a thermal cloud remains, however, with a temperature below the recoil limit ($T < 0.2 E_r/k_B \approx 30$ nK).

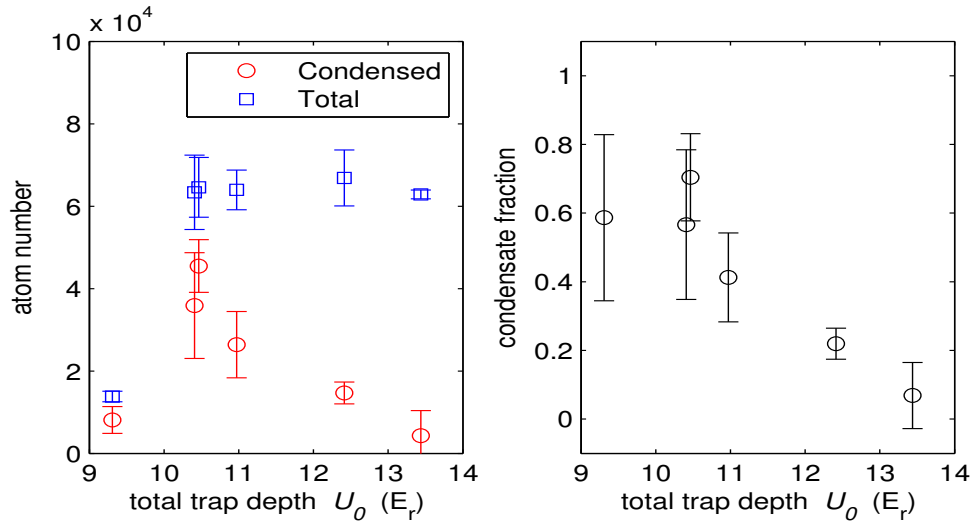


Figure 4.11.: HOLDING THE BEC IN THE LATTICE: The BEC is loaded into the standing wave within 120 ms, held for 500 ms and then loaded back into the magnetic trap in 100 ms. After release from the magnetic trap, (a) the total number and number of condensed atoms and (b) the condensate fraction are measured as a function of the lattice depth.

for an approximately $10 E_r$ deep trap, where we lose about 65% of the atoms, but maximize the condensate fraction (see Fig. 4.11). Because high lattice intensities are detrimental for the BEC, we readjust the power of the lattice during transport, such that the intensity is kept constant over the transport range. The adjustments are based on the calculated axial intensity distribution of the Bessel beam. In this way we reach transport distances for BEC of 10 cm. We believe, that more sophisticated fine tuning of the power adjustments should increase the transport length considerably. After transport distances of $D = 18$ cm (36 cm round trip) the atomic cloud is thermal. Its momentum spread, however, is merely $0.3 \hbar k$, which corresponds to a temperature of 30 nK. Additionally, we want to point out, that the loss of atoms due to the transport is negligible ($<10\%$) compared to the loss through loading and simply holding in such a low lattice potential ($\approx 65\%$).

4.2.5. Prominent features of the transport

In this section some basic properties of the transport are discussed. We will present measurements, which show, how fast and how accurately the atoms may be relocated.

Precise Positioning An outstanding feature of the lattice transport scheme is the precise positioning of the atomic cloud (Fig. 4.12). Aside from uncontrolled phase shifts due to moving mirrors etc. we have perfect control over the relative phase of the lattice lasers with our RF / AOM setup. This would in principle result in an arbitrary accuracy in positioning the optical lattice. We have experimentally

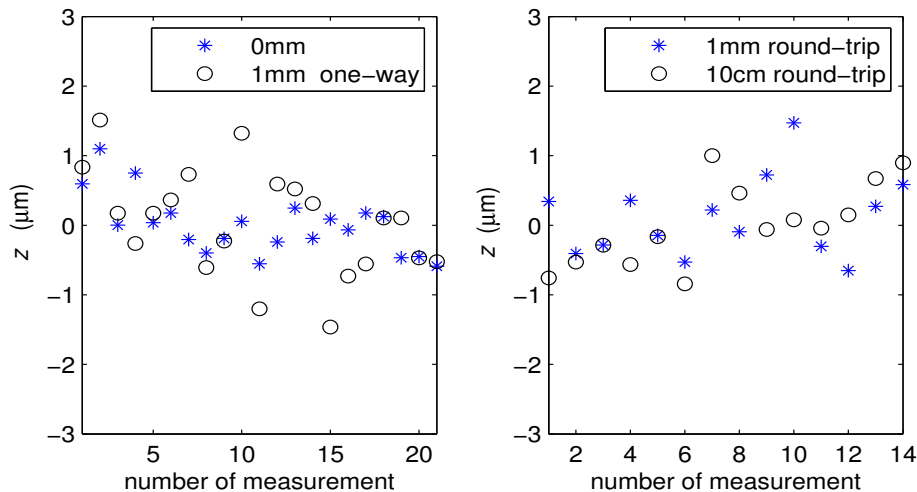


Figure 4.12.: ACCURATE POSITIONING OF THE CLOUD: The axial position z of the cloud is determined by in-situ imaging the atoms before and right after the transport, respectively. The value $z = 0$ corresponds to the mean position. The measured standard deviation from the mean position is $0.4 \mu\text{m}$, $0.8 \mu\text{m}$, $0.7 \mu\text{m}$ and $0.6 \mu\text{m}$ for transports over 0 mm, 1 mm one-way, 1 mm round-trip and 10 cm round-trip, respectively. All four series of measurements were done independently and therefore there are no correlations between them.

investigated the positioning capabilities in our setup. For this we measured in many runs the position of the atomic cloud in the lattice after it had undergone a return trip with a transport distance of up to $D = 10$ cm (Fig. 4.12). A slight increase of the position jitter due to the transport is observed, even though the order of magnitude of the jitter ($\sim 1 \mu\text{m}$) stays the same. Here we want to point out, that this measurement of the position jitter is in nice agreement with the phase drift measurement presented before (Fig. 4.5).

Small transport durations Another important property of the lattice transport scheme is its short durations. For example, for a transport over 20 cm (40 cm round trip) with negligible loss, a total transport time of 200ms is sufficient. This is more than an order of magnitude faster than in the MIT experiment, where an optical tweezer was mechanically relocated [Gus02]. The reason for this speed up is the much higher axial trapping frequency of the lattice as compared to the optical tweezer, in combination with the fact, that no mechanical relocation of any part of the experiment is required.

High accelerations In order to determine experimentally the lower limit of transportation time we have investigated round-trip transports ($D = 5$ mm), where we have varied the maximum acceleration and the lattice depth (Fig. 4.13 a). The number of atoms, which still remain in the lattice after transport, is measured. As the

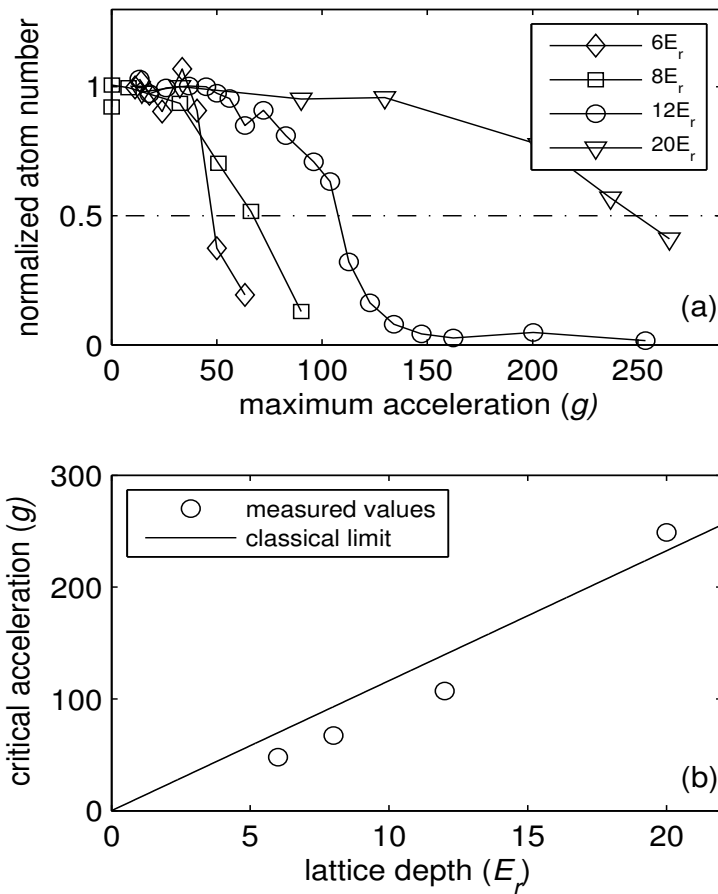


Figure 4.13.: CRITICAL ACCELERATION IN LATTICE. **(a)** Every transport over a given distance D within a given duration T can be associated with a well-defined maximum acceleration, experienced by the atoms during this transport process. Therefore the atom number may easily be measured as a function of maximum acceleration by varying the transport duration T . As the maximum acceleration exceeds a critical value, the number of atoms starts to drop. We define a critical acceleration as the maximum acceleration for transports in which 50% of the atoms still reach their final destination. This critical acceleration is shown as a function of the lattice depth in **(b)**. The experimentally determined values are compared with the limit expected from classical considerations: $a_{crit} = U_{latt}k/m$.

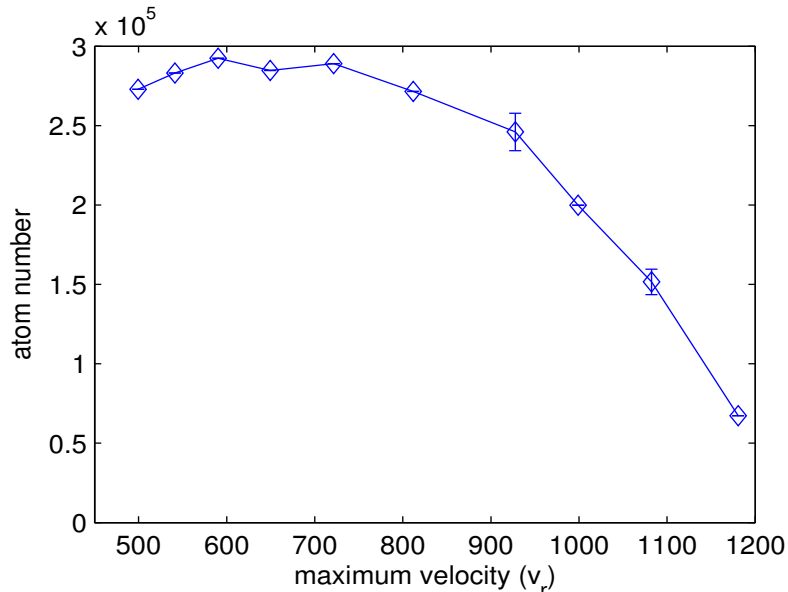


Figure 4.14.: Atom number as a function of the maximum velocity during transport.

maximum acceleration exceeds a critical value, the number of atoms starts to drop. We define a critical acceleration a_{crit} as the maximum acceleration for transports in which 50% of the atoms still reach their final destination. Figure 4.13b shows the critical acceleration a_{crit} as a function of lattice depth. The upper bound on acceleration can be understood from classical considerations (section 3.1). As seen, in order to keep an atom bound to the lattice, we require the acceleration a to be small enough such that

$$ma < U_{latt}k. \quad (4.9)$$

Our data in Fig. 4.13 are in good agreement with this limit.

As discussed in the previous chapter one also expects a lower bound on acceleration $a > 0.6 \text{ m/s}^2$, due to instabilities. However, in our transport experiments we have not seen any indications of instabilities. The reason is probably, that for the most part of the transport the acceleration clearly exceeds this value.

High velocities In contrast to acceleration, the transport velocity in our experiment is only limited due to a technical reason, namely the AOM bandwidth. As discussed before, the lattice is set in motion by introducing a detuning between the two beams via AOMs (equation (3.35)). For detunings exceeding the bandwidth of such an AOM, the diffraction efficiency of the modulator starts to drop significantly. Consequently the lattice confinement vanishes and atoms are lost. In our experiment we can reach velocities of up to $v = 6 \text{ m/s} \approx 1100 v_r$ (see Fig. 4.14), corresponding to a typical AOM bandwidth of 15 MHz. This upper bound actually limits the transport time for long distance transports ($D > 5 \text{ cm}$).

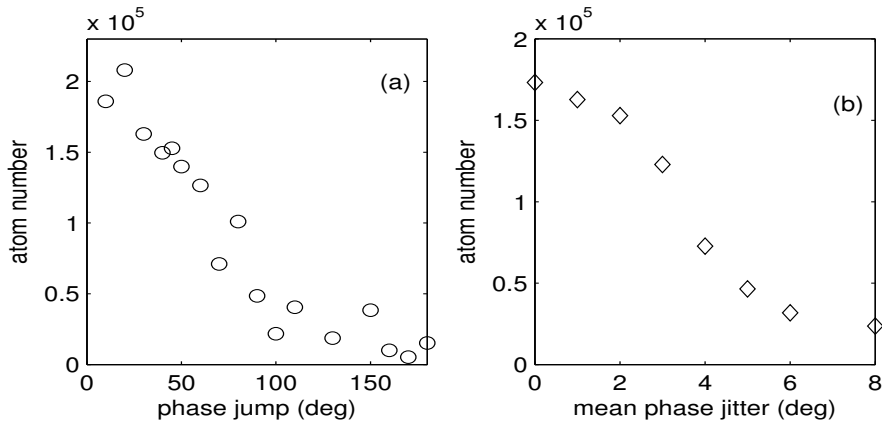


Figure 4.15.: STABILITY REQUIREMENTS FOR TRANSPORT. Sudden phase jumps are introduced in the relative phase of the two counterpropagating lattice laser beams. The corresponding abrupt displacements of the optical lattice lead to heating and loss of the atoms. We measure the number of atoms which remain in the lattice after transport. **(a)** Data obtained after a single relative phase jump of variable magnitude. **(b)** A phase jitter (200 positive Poissonian-distributed phase jumps with a variable mean value) is introduced during transport. Mean values on the order of a few degrees already lead to a severe loss of atoms.

Phase noise As discussed, slow phase drifts of the lattice lead to position drifts of the atomic cloud. In order to further investigate the influence of phase noise, sudden phase jumps during transport are introduced to one of the lattice beams. The timescale for the phase jumps, as given by AOM response time of about 100 ns, was much smaller than the inverse trapping frequencies. The phase jumps lead to abrupt displacements of the optical lattice causing heating and loss of atoms. Figure 4.15 shows two data sets. The first one explores atomic losses due to a single phase jump during transport. Phase jumps of 60 degrees typically induce a 50 % loss of atoms. For a continuous phase jitter (here: 200 positive Poissonian-distributed phase jumps with a variable mean value) the sensitivity is obviously much larger (Fig. 4.15(b)).

4.3. Atom catapult

In addition to transport of ultracold atoms, acceleration of atoms to precisely defined velocities is another interesting application of the moving optical lattice. For instance, it could be used to study collisions of BECs with a very high but well defined relative velocity, similar to the experiments described in [Tho04, Bug04]. As already shown above, we have precise control to impart a well defined number of up to 1100 photon recoils to the atoms. This corresponds to a large kinetic energy of $k_B \times 200$ mK. At the same time the momentum spread of the atoms is about 1/3 of a recoil (see Figure 4.10).

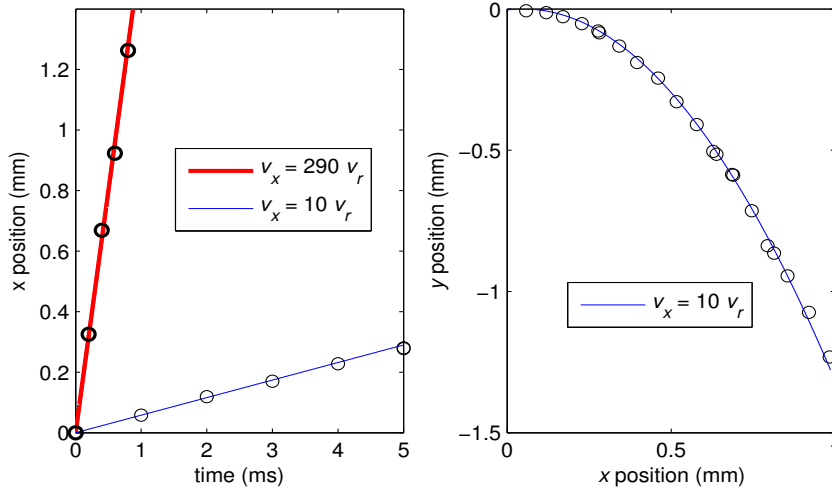


Figure 4.16.: ATOM CATAPULT. After acceleration in x -direction and subsequent release from the lattice, the position of the atomic cloud is tracked as it flies freely through the field of view of the CCD camera. Shown are two data sets where atoms were accelerated to velocities of either $v_x = 10 v_r$ or $v_x = 290 v_r$. **(a)** The horizontal position x as a function of time. **(b)** For the slower cloud ($v_x = 10 v_r$) a parabolic trajectory $y = -g/2(x/v_x)^2$ is observed as it falls under the influence of gravity.

To illustrate this, we have performed two sets of experiments, where we accelerate a cloud of atoms to velocities $v = 10 v_r$ and $v = 290 v_r \approx 1.6$ m/s. After adiabatic release from the lattice, we track their position in free flight (see Figure 4.16). Initially the atomic cloud is placed about 8 cm away from the position of the magnetic trap. It is then accelerated back towards its original location. Before the atoms pass the camera's field of vision, the lattice beams are turned off within about 5 ms, to allow a ballistic flight of the cloud. Using absorption imaging the position of the atomic cloud as a function of time is determined. The slope of the straight lines in Figure 4.16(a) corresponds nicely to the expected velocity. However, due to a time jitter problem, individual measurements are somewhat less precise than one would expect. We believe that this is linked to the fact that our clock for the system control is synchronized to the 50 Hz of the power grid, whereas the clock for the RF synthesizers are not. We know, that the relative fluctuations of the 50 Hz line frequency are on the order of 10^{-3} . For the atom catapult experiment with a duration of about 200 ms these fluctuations lead to shot to shot variations in the ballistic flight time of the atoms of about $200 \mu\text{s}$ (see Fig. 4.16(a)).

For $v = 10 v_r$, Figure 4.16(b) shows the trajectory of the ballistic free fall of the atoms in gravity.

5. Conclusion & Outlook

This diploma thesis describes the first experiment, in which a moveable standing wave dipole trap is used to transport ultracold atoms over macroscopic distances (exceeding the cm range). By using a standing wave the momentum of the atoms is controlled on the quantum level (uncertainty less than $2\hbar k$) at any instant of time. The novelty of this experiment is the utilization of diffraction-free Bessel beam, with which transport over principally arbitrary distances may be realized. In our case we were able to move BECs over several cm and ultracold atoms ($T < E_T/k_B$) over up to 20 cm. By the use of an refractive axicon, Bessel beams can be produced in a very simple and efficient way. In comparison to other schemes, the lattice transport features fast and accurately controllable transport speeds ($1100(1)v_r$), high accelerations (2600 m/s^2) and high positional accuracy ($1\ \mu\text{m}$).

Many limitations are technical and leave large room for improvement. For instance the maximum speed of $1100 v_r$ could be increased by a factor of 2, in case the detuning between the two beams is introduced via a double-pass AOM configuration. Another example is the size and therefore the Rayleigh range of the Gaussian beam, which was chosen rather small, due to time constraints. Increasing them would be fairly easy and would help to enlarge the axial range of the lattice. In the end the range of the Bessel beam and thus the transport range may be extended significantly by providing more total power.

The presented transport technique is a possible method to separate the place of BEC production from the location, where the condensate is probed. Furthermore the numerous features described in the text, make this scheme a good candidate for loading BECs onto atom chips or into high finesse cavities.

In addition to transport, the lattice can also be used as an accelerator to impart a large but well defined number of photon recoils to the atoms. Such an experiment for example could be used to study the collision between two BECs.

A. Digital radio-frequency synthesizers

For our experiment we require two phase-locked radio-frequency sources, which may put out arbitrary amplitude and frequency ramps. A device, meeting those demands, was developed and built in our group by Manfred Mark and Gregor Thalhammer. Since the transport experiment discussed in this thesis is one of the first applications of these digital synthesizers, I want to use this appendix to explain their functionality in more detail.

Frequency generator

The heart of this RF source is the frequency generator board AD9854, which may generate RF signals with a resolution of $1 \mu\text{Hz}$ for frequencies up to 150 MHz. A functional block diagram with an explanation of the basic functionality is shown in Fig. A.1. The synthesizer is based on the DDS principle, which works as follows. The goal is to create a signal S of the form $S = \sin(2\pi f(t)t)$. The main task is to calculate the phase $\phi = ft$. This is done via the recursion relation $\phi(t_{n+1}) = \phi(t_n) + \delta\phi$, where $t_n = n\tau$, with the fixed time increment τ and an integer number n . The phase increment $\delta\phi$ is given by $\delta\phi = f\tau$ and therefore determines the frequency f of the output signal. The recursion is implemented digitally, using an adder and a couple of registers. A nice picture for a better understanding of this procedure is the phase wheel shown in Fig. A.2(a). After performing the recursion, an additional phase-offset $\varphi(t_n)$ may be added, leading to a signal $S = \sin(2\pi ft + \varphi)$. This signal S is multiplied with the desired amplitude A_n and then sent through a D/A converter. After filtering, the output power of the signal is about -12 dBm. The signal is amplified by more than 40 dB and then sent to the AOM.

The frequency of the RF signal produced with the DDS technique may be adjusted very precisely and changed very fast over a wide range. Furthermore the RF wave does not exhibit unwanted phase jumps, even when the frequency is changed abruptly (Fig. A.2(b)). Last but not least the AD9854 is synchronized to an external reference oscillator (X0-105BIC @ 60.000000 MHz), which allows to phase lock several AD9854 to each other.

A clear disadvantage of the chip is the fact, that it only comes with a few working registers and input buffers and does not have the intelligence to create complex amplitude or frequency ramps. For this reason we use a micro-controller, on which arbitrary ramps may be stored.

Micro-controller

The micro-controller used here is a ATMega162 from Atmel. It is equipped with a 8-bit processor as well as 16 kByte flash-memory, 1 kByte SRAM and 512 Byte EEPROM.

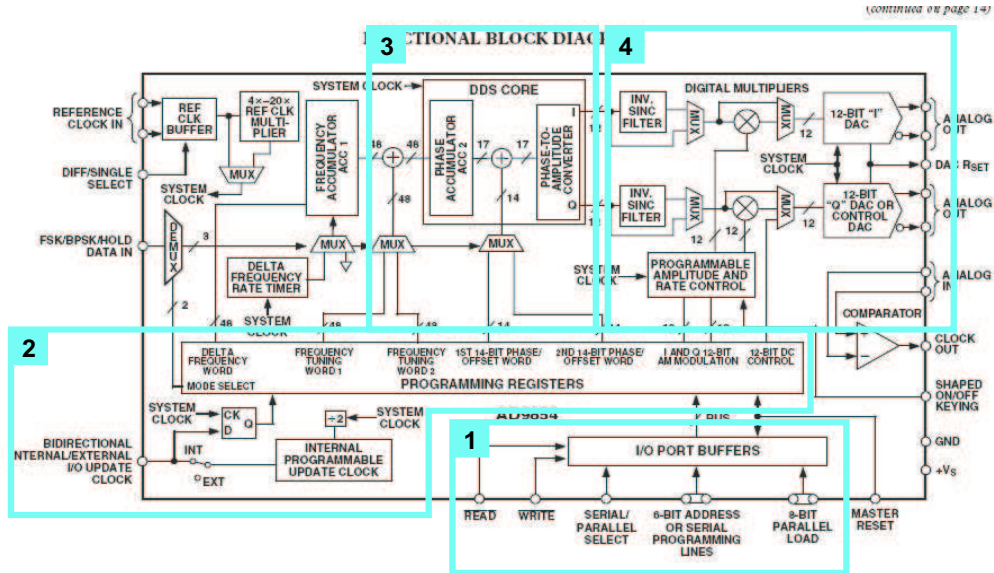


Figure A.1.: FUNCTIONAL BLOCK DIAGRAM OF THE AD9854: (1) **Loading of the I/O buffer:** The values for amplitude, frequency and phase are stored in an intermediate memory (the I/O buffer) via a parallel interface. (2) **Loading the register:** Triggered by the I/O update signal, the values are transferred to the main register of the chip. (3) **DDS core:** The DDS core is the heart of the entire device (see explanation in the text) (4) **Amplitude control:** The signal value S is multiplied with an amplitude value and then sent through a DA-converter so that we end up with with an analog output signal.

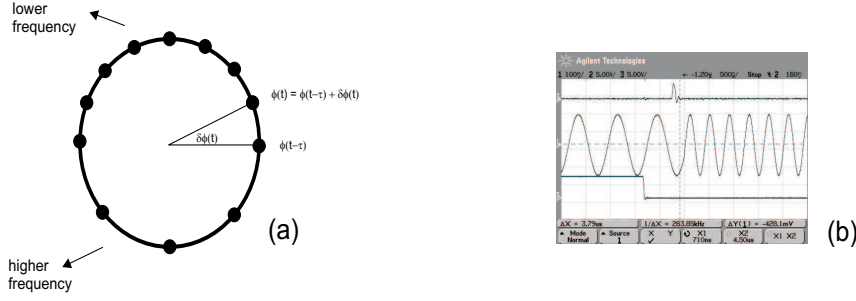


Figure A.2.: **(a)** Digital phase wheel: The phase wheel represents the recursion formula modulo 2π . The phase increment $\delta\phi$ determines the frequency of the RF wave via $\delta\phi = f\tau$. As an example a phase wheel is shown, where the second half period is run through with twice the frequency as compared to the first half period. **(b)** The corresponding RF signal: Even though the frequency is doubled all of a sudden, the signal stays continuous (no phase jump).

Additionally a 32 kByte external RAM is implemented. The size of the RAM is sufficient to store ramps with up to $N \simeq 1200$ data points (for each amplitude, frequency and phase) on it. For both, the external RAM as well as the communication with the synthesizer (AD9854) a parallel interface is used. The speed of the communication between the μ -controller and the AD9854 is determined by the time to load one data point (about 20 Byte) from the input buffer into the working register. Since this only takes a few μ s, fast communication of more than 2 MByte/s is possible.

The ramps are created in Matlab. They are first saved in a *.bin file on the PC and then stored on the μ -controller using a short Python program (“laden.py”). The communication between the PC and the micro-controller is established with a RS232 interface. This kind of link consists of a USB plug on the computer side and a serial port for the connection with the micro-controller.

Frequency and Amplitude ramp

By using Matlab, the desired ramps are generated in the form of vectors. The user puts in the total ramp time T and vectors for amplitude A , frequency f and an additional phase shift φ . For the transport experiments phase coherence is required and so the phase shift φ is set to zero for all times. In addition to this manually generated vectors, the m-file itself also creates a time vector t and a frequency difference vector Δf (= a vector, whose entries are the difference between neighboring entries of the frequency vector: $\Delta f_n = f_{n+1} - f_n$). These vectors then merge to a single matrix of the form

$$\begin{pmatrix} t_1 & A_1 & f_1 & \Delta f_1 & \varphi_1 \\ \vdots & \vdots & \vdots & \vdots & \vdots \\ t_n & A_n & f_n & \Delta f_n & \varphi_n \\ \vdots & \vdots & \vdots & \vdots & \vdots \\ t_N & A_N & f_N & \Delta f_N & \varphi_N \end{pmatrix} \quad (\text{A.1})$$



Figure A.3.: Basic idea for generating the frequency and amplitude ramps: Amplitude and frequency ramps are programmed on a PC and stored on a microcontroller (μC). Upon request they are then sent to the AD9854, which generates the corresponding RF signal.

where the n -th line of this matrix gives information on amplitude, frequency and phase at the time t_n . The values for amplitude and phase can only be changed stepwise, with the time increments $t_{n+1} - t_n$ being at least $10 \mu s$ (limited by the time the AD9854 needs to process one data point). However, the frequency can be interpolated linearly between f_n and f_{n+1} , resulting in extremely smooth frequency ramps. The only requirement for this is, that Δf_n is also sent to the synthesizer, since it does not know the value f_{n+1} at the time t_n .

Once the values for the matrix (A.1) are set, the corresponding binary numbers are calculated (using the Matlab function 'num2bin'). The data point, which is sent to the μ -controller, then contains two 6 Byte numbers for each the frequency and for the difference frequency, as well as two 2 Byte numbers for the amplitude and the phase shift of the signal.

B. Phase Stabilization of Diode Lasers

B.1. Introduction

This appendix describes a work performed independently from the transport experiment discussed throughout this thesis. The goal here was to establish a phase-lock between two diode lasers, whose frequencies may differ by up to 6 GHz. This is achieved by determining the phase between the two lasers via a beat measurement. After readjusting its gain, this phase error signal is fed back to the current of one of the lasers. Eventually more than 90% of the light was phase-locked, corresponding to a residual phase error of $\Delta\phi_{rms} \simeq \frac{\pi}{10}$.

B.2. Feedback circuitry

In the field of electronics the idea of feedback is a very important tool for the stabilization of certain parameters such as e.g. the temperature of an oven or the frequency of a laser. The basic idea [Hor89] of such circuits is shown in Fig. B.1.

Y_A, Y_B, Y_C and Y_D are the signals in the frequency domain, that is, the Fourier-Transforms of the respective signals in the time domain.

$$Y_i(\omega) = \int_0^\infty y_i(t)e^{-i\omega t} dt \tag{B.1}$$

The signals are commonly named as following: the output of the system Y_A , the reference signal Y_B , the error signal Y_C and the input into plant Y_D . The plant is the device, which has to be stabilized. It is characterized by the transfer function $A(\omega)$. The transfer function of the controller is labeled $B(\omega)$. When the transfer functions are known,

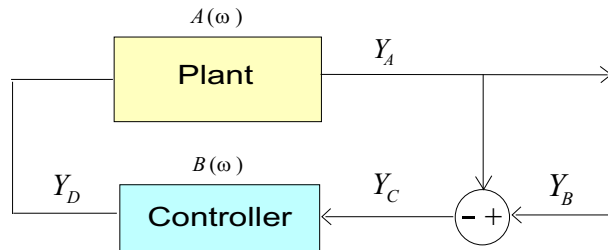


Figure B.1.: Basic scheme of a feedback circuit.

simple relations between the signals Y_i exist.

$$\begin{aligned} Y_C(\omega) &= Y_B(\omega) - Y_A(\omega) \\ Y_D(\omega) &= B(\omega)Y_C(\omega) \\ Y_A(\omega) &= A(\omega)Y_D(\omega) \end{aligned} \tag{B.2}$$

Thus the transfer function of the whole feedback loop may be written as

$$H(\omega) := \frac{Y_A}{Y_B} = \frac{A(\omega)B(\omega)}{1 + A(\omega)B(\omega)} \tag{B.3}$$

B.3. Phase locked loops

The feedback idea from above is now applied to the stabilization of an voltage-controlled oscillator (VCO). The goal of a phase locked loop (PLL) is to stabilize not only the frequency, but also the phase of the oscillator. Therefore a phase-sensitive signal is needed. Such a signal is gained by multiplying the signal of the VCO with that of a stable local oscillator (LO). The signals are given by

$$\begin{aligned} V_{vco}(t) &= V_1 \cdot \sin(\omega_{vco}(t)t + \varphi_{vco}(t)) \\ V_{lo}(t) &= V_2 \cdot \cos(\omega_{lo}t + \varphi_{lo}) \end{aligned} \tag{B.4}$$

Multiplication leads to

$$\begin{aligned} V_{vco}(t) \cdot V_{lo}(t) &= V_1 V_2 \sin(\omega_{vco}(t)t + \varphi_{vco}(t)) \cdot \cos(\omega_{lo}t + \varphi_{lo}) \\ &= \frac{V_1 V_2}{2} \sin([\omega_{vco}(t) + \omega_{lo}]t + \varphi_{vco} + \varphi_{lo}) + \\ &\quad \frac{V_1 V_2}{2} \sin([\omega_{vco}(t) - \omega_{lo}]t + \varphi_{vco} - \varphi_{lo}) \\ &\simeq \frac{V_1 V_2}{2} \sin([\omega_{vco}(t) - \omega_{lo}]t + \varphi_{vco} - \varphi_{lo}) \end{aligned} \tag{B.5}$$

The term in the second line cancels after performing a time average over a cycle of period $T = \frac{2\pi}{\omega_{lo}}$

$$\begin{aligned} \sin([\omega_{vco}(t) + \omega_{lo}(t)]t + \varphi_{vco} + \varphi_{lo}) &\simeq \sin(2\omega_{lo}t + \varphi_{vco} + \varphi_{lo}) \\ \frac{1}{T} \int_0^T \sin(2\omega_{lo}t + \varphi_{vco} + \varphi_{lo}) dt &= 0 \end{aligned}$$

From equation (B.5) it can be seen, that stabilizing $V_{vco}(t) \cdot V_{lo}(t)$ to zero will stabilize the frequency difference $\omega_{vco} - \omega_{lo}$ and the phase difference $\varphi_{vco} - \varphi_{lo}$ to zero. Therefore $V_{vco}(t) \cdot V_{lo}(t)$ could be used as an error signal for the phase stabilization.

A simple realization of a PLL is shown in Fig. B.2. The multiplication is performed with a mixer. The mixer is followed by a low-pass filter (LP), which averages out the

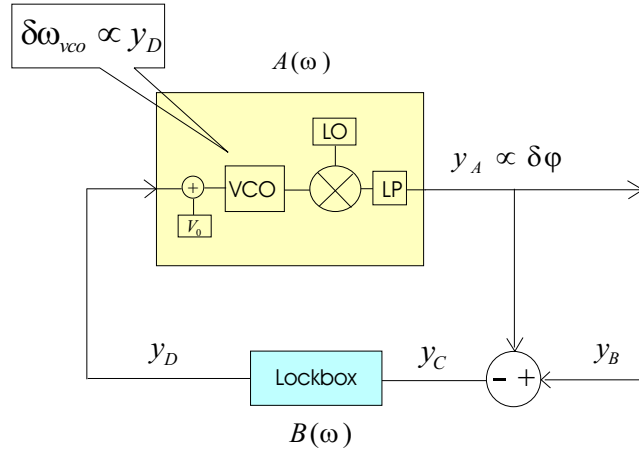


Figure B.2.: Schematic of a phase locked loop (PLL).

rapid oscillations (at $2\omega_{lo}$). The VCO is controlled by the voltage V_0 plus the input signal y_D . When the system is stabilized, $y_A = y_B$ and $y_D = 0$. Small perturbations (e.g. due to the finite phase stability of the VCO) then change the output signal y_A and consequently the input y_D . The frequency of the VCO then gets shifted by small amount $\delta\omega_{vco}$, proportional to y_D . Now the integrating behavior of a VCO-type plant becomes visible: The input y_D is proportional to the frequency of the VCO, where as the output y_A is proportional to the phase. We can write

$$\begin{aligned}\delta\omega_{vco}(t) &= C_1 \cdot y_D(t) \\ y_A(t) &= C_2 \cdot \delta\varphi_{vco}(t)\end{aligned}\quad (\text{B.6})$$

$$\begin{aligned}\int_0^t y_D(t)dt &= \frac{1}{C_1} \int_0^t \delta\omega_{vco}(\bar{t})d\bar{t} \\ &= \frac{1}{C_1} \cdot \delta\varphi_{vco}(t) \\ &= \frac{1}{C_1 C_2} \cdot y_A(t) = \frac{1}{C} \cdot y_A(t)\end{aligned}\quad (\text{B.7})$$

Performing a Fourier-Transformation on both sides, leads to

$$\frac{Y_D(\omega)}{i\omega} = \frac{1}{C} Y_A(\omega)\quad (\text{B.8})$$

Thus the transfer function of the plant is given by

$$A(\omega) = \frac{Y_A(\omega)}{Y_D(\omega)} = \frac{C}{i\omega}\quad (\text{B.9})$$

where the constant C characterizes the VCO.

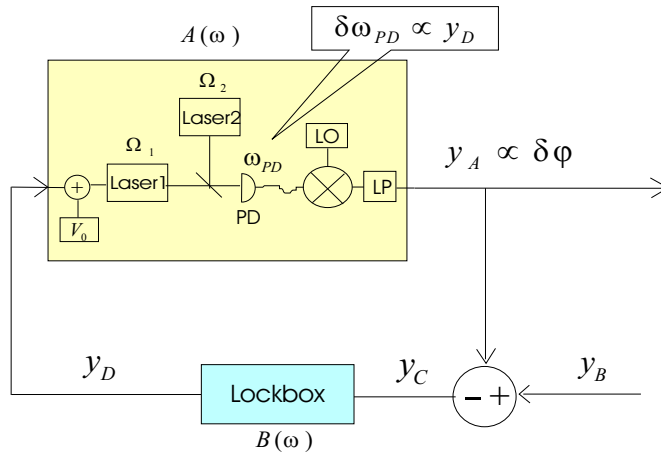


Figure B.3.: PLL with two diode lasers: The beat note at frequency $\omega_{PD} = \Omega_1 - \Omega_2$ between two diode lasers is detected with a photo diode (PD). This beat signal is then mixed with a LO, running at the desired frequency difference between the two lasers. Assuming a stable LO, the output (after the LP) is then proportional to the phase error between the two lasers.

B.4. Phase locked diode lasers

The PLL scheme from above can readily be applied to the case, where the relative phase of two lasers is stabilized (Fig. B.3). The input y_D is then modulating the current through one of the laser diodes. Consequently also the frequency of this laser and the frequency of the beat signal between the lasers changes with the input signal y_D . Thus the two lasers together with the beat-detection are equivalent to the VCO; i.e. the beat signal is phase stabilized with such a setup. And a phase stable beat signal of course implies that the relative phase between the two lasers is stable.

However, one has to point out, that lasers are *not ideal* VCOs. As we will see below (Fig. B.6 and Fig. B.5), the simple linear relation $\delta\omega_{VCO}(t) = C_1 \cdot y_D(t)$ does not hold for the high frequency components of $y_D(t)$. The response of the laser C_1 is not constant, but drops for frequencies $(\omega/(2\pi) \geq 100 \text{ kHz})$.

B.4.1. Diode lasers

In the experiments discussed here home-built external cavity diode lasers (ECDL) [Har91, Mac92] are used. The diodes are AlGaAs laser diodes from Laser Components (RLD78PZW2). The frequency of such an ECDL can be modulated with either the current sent through the diode, or by tuning the external cavity with a piezo-electric transducer (PZT). In Fig. B.5 and Fig. B.6 the frequency response to current and PZT modulation, respectively, is shown. To gain this so-called Bode diagram the current is modulated with a sinusoidal signal $V_{in} = V_{0,in} \cos \omega t$. The response of the laser frequency is measured via a beat with a second laser. This beat frequency f is converted into a voltage using a

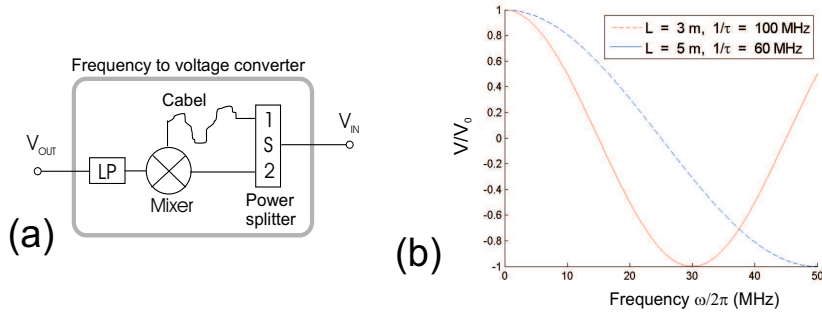


Figure B.4.: **(a)** Frequency to voltage converter as described in the text. **(b)** The output signal V_{out} of the RF interferometer as a function of frequency $\omega/(2\pi)$ for two different delay lines. The bandwidth is $1/(2\tau) = 50$ MHz and $1/(2\tau) = 30$ MHz, respectively.

RF interferometer, which consists of a power splitter, a frequency mixer and a low-pass filter (Fig. B.4(a)) is a fairly simple way to convert a frequency into a voltage. After splitting, one of the signals goes directly to the mixer, where as the other one has to travel through a delay line of length L . The output of the mixer is then given by

$$\begin{aligned} V_{\text{out}} &= 2V_0 \cdot \cos(\omega t) \cdot \cos(\omega(t + \tau)) \\ &= V_0 \cdot [\cos(\omega(2t + \tau)) + \cos(\omega\tau)] \end{aligned} \quad (\text{B.10})$$

with the delay time $\tau = \frac{L}{c}$. After low-passing

$$V_{\text{out}}(f) = V_0 \cdot \cos \omega\tau \quad (\text{B.11})$$

Within the frequency range of $BW_{\text{RFint}} \simeq \frac{1}{2\tau}$ the output voltage is approximately proportional to the frequency f of the input signal (Fig. B.4(b)). Thus for small V_{in} the ratio $\frac{V_{\text{out}}}{V_{\text{in}}}$ reflects the frequency response of our laser.

As can be seen from Fig. B.5, the current of the laser may be easily modulated with up to a few hundred kHz. For frequencies above 1 MHz the gain already drops by a factor of two and the phase delay already exceeds 90° . As we will see later, this is one major reason, why the bandwidth of our entire PLL is limited to about 1 MHz.

Fig B.6 on the other hand shows, that the bandwidth of the PZT channel is about 3 kHz. The first large resonance at about 3.6 kHz can be filtered out with a notch filter. However, this will not increase the bandwidth by orders of magnitudes, since further resonances follow. The fairly small resonance at about 200 Hz does not have a big influence on the performance of the lock.

Now that the frequency response of the laser is known, one can write down the more realistic version of the transfer function $A(\omega)$ for the phase lock (compare with equation B.9).

$$A(\omega) = \frac{C}{i\omega} \cdot \frac{V_{\text{out}}(\omega)}{V_{\text{in}}} \quad (\text{B.12})$$

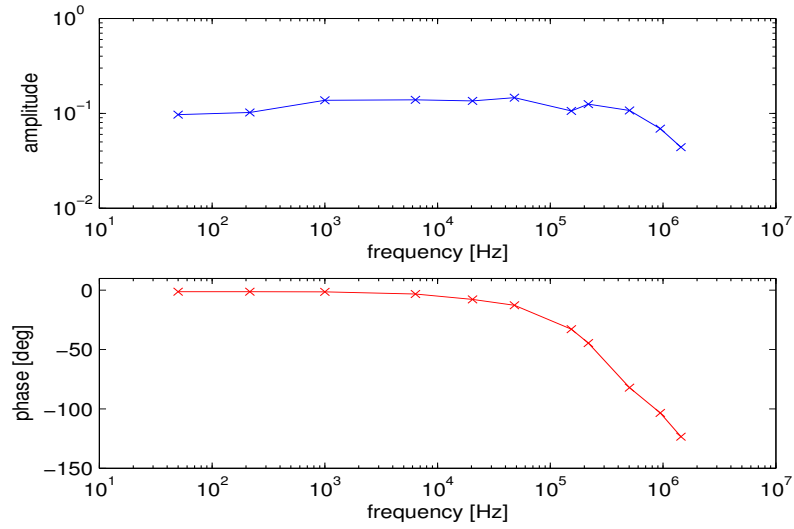


Figure B.5.: Bode diagram for the current modulation of a diode laser: The gain $G = \left| \frac{V_{\text{out}}}{V_{\text{in}}} \right|$ and the phase $\varphi = \arg \left(\frac{V_{\text{out}}}{V_{\text{in}}} \right)$ are plotted versus the modulation frequency ω .

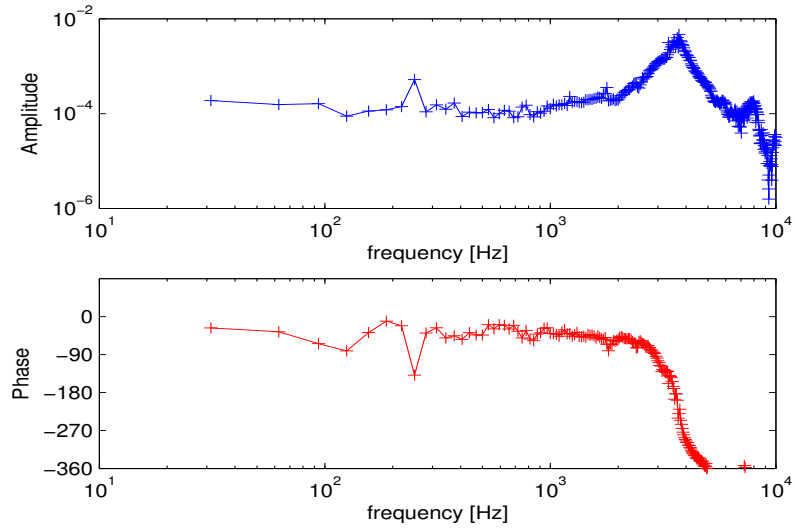


Figure B.6.: Bode diagram for the modulation of the PZT: The gain $G = \left| \frac{V_{\text{out}}}{V_{\text{in}}} \right|$ and the phase $\varphi = \arg \left(\frac{V_{\text{out}}}{V_{\text{in}}} \right)$ are plotted versus the modulation frequency ω .

Another important property for phase locking is the individual coherence of the two lasers. A direct measure for the coherence is the spectral width of the laser light. To determine the linewidth of the ECDLs used here, the beat note between the two lasers, running independently at similar frequencies, is detected. In Fig. B.7 the spectrum of this signal is shown. The shape of the power spectrum $P(\omega)$ is well described by the so-called Voigt profile, which is a convolution between a Lorentzian and a Gaussian profile

$$P(\omega) \propto \int_{-\infty}^{\infty} d\bar{\omega} e^{-\left(\frac{\bar{\omega}-\omega_0}{\Delta\omega_G}\right)^2} \frac{1}{1 + \left(\frac{\omega-\bar{\omega}-\omega_0}{\Delta\omega_L}\right)^2} \quad (\text{B.13})$$

where ω_0 is the beat frequency and $\Delta\omega_G$ and $\Delta\omega_L$ are the widths of the Gaussian and the Lorentzian part, respectively. The widths are given by

$$\begin{aligned} \Delta\omega_G^2 &= \Delta\omega_{G,\text{laser1}}^2 + \Delta\omega_{G,\text{laser2}}^2 \\ \Delta\omega_L^2 &= \Delta\omega_{L,\text{laser1}}^2 + \Delta\omega_{L,\text{laser2}}^2 \end{aligned} \quad (\text{B.14})$$

with $\Delta\omega_{G,\text{laser1,2}}$ and $\Delta\omega_{L,\text{laser1,2}}$ being the widths of the Voigt profiles of the individual lasers. The relations (B.14) arise from the fact, that the convolution of two Gaussians/Lorentzians is again a Gaussian/Lorentzian, with the width given by the quadratic sum of the original two Gaussians/Lorentzians.

Since both ECDL are of the same type and are operated with the same laser diode, we assume approximately the same spectral width for both lasers $\Delta\omega_{G,\text{laser1}} \approx \Delta\omega_{G,\text{laser2}} = \Delta\omega_{G,\text{laser}}$. Then the laser linewidth may be derived from the width of the beat signal (Fig. B.7)

$$(\Delta\omega_{G,\text{laser}}, \Delta\omega_{L,\text{laser}}) = \frac{1}{\sqrt{2}}(\Delta\omega_G, \Delta\omega_L) = 2\pi(420 \text{ kHz}, 20 \text{ kHz}) \quad (\text{B.15})$$

One major reason, why we reach linewidths in the sub-MHz range is the use of an external cavity diode laser (ECDL). Both, the internal (= the facets of diode itself) and the external resonator (grating) have a finesse of about 3. However, since the length of the external cavity is more than a factor of ten larger than the internal one, the corresponding linewidth is reduced by more than an order of magnitude.

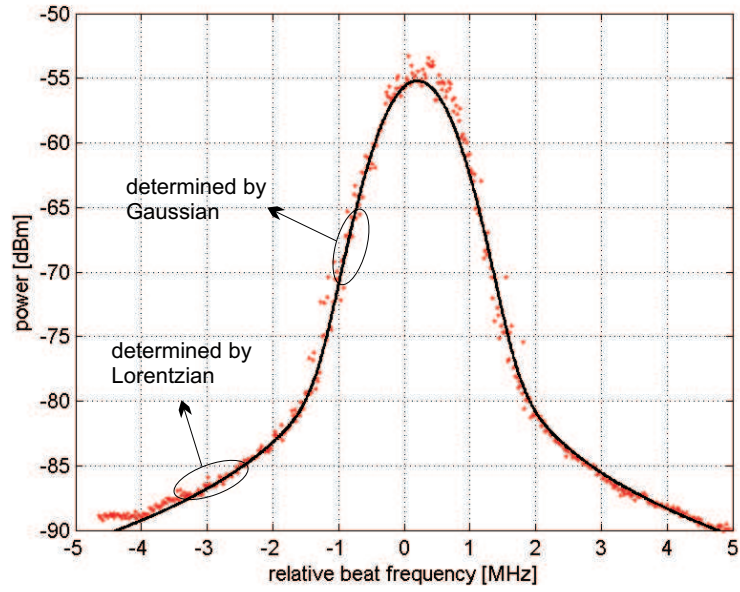


Figure B.7.: Beat between two free-running external cavity diode lasers. The beat frequency here is 1 GHz, however, the frequency axis is shifted such that the peak appears at zero frequency. A convolution between a Gauss with $\Delta\omega_G = 2\pi \times 600$ kHz and a Lorentz with $\Delta\omega_L = 2\pi \times 33$ kHz is fitted to the data. As indicated, the Gaussian part is responsible for the initial drop of the signal close to the center, whereas the long-range wings are due to the Lorentzian part.

B.4.2. Lockbox

At the input of the lockbox (Fig. B.8) the error signal is split into two channels: The PZT channel (lower part in Fig. B.8) is basically a simple PI controller (IC's 1, 2 and 3) plus an optional inverter (IC4). The notchfilter at the output filters out the lowest mechanical resonance of the PZT, so that the overall gain of this channel can be further increased. Similarly there is a PI controller for the current channel (IC's 5 and 6). In between these two chips the signal is split into a medium fast and a very fast branch. The medium fast one is simply a low pass filter with a cut-off frequency of 170 kHz. For frequencies above this cut-off the frequency response of the laser is not instantaneous any more; i.e. the phase shift exceeds 90° (Fig.B.5). The low pass filter is installed to avoid significant feedback at frequencies, where the phase shift reaches 180° . If we just had the medium fast branch for our current channel, the bandwidth of the phase locked loop would approximately given by the cut-off of 170 kHz. This is on the same order (or even lower) than the laser linewidth and thus insufficient for phase locking. (Rule of thumb: The bandwidth of the PLL should be at least four times larger than the linewidth of the laser.) For this reason an additional high-speed branch is added. The idea here is to have a passive loop filter that shifts the phase forward. This shift forward can then compensate for the low pass like behavior of the laser diode itself. In this way the phase shift stays below 90° for frequencies up to the MHz region, which makes feedback up to this frequencies possible.

B.4.3. Experimental setup

In Fig. B.9 the details of the setup are shown. The beams of the two ECDL are overlapped with a 50/50 beamsplitter and the beat is detected with a Metal-Semiconductor-Metal (MSM) photo-detector (PD) from Hamamatsu (model G4176). This signal is amplified (A1) with two microwave amplifiers from Minicircuits (ZJL-6G) and then mixed with a stable tunable microwave source (HP 8341A). M1 is a frequency mixer from Minicircuits (model ZEM-4300 or ZMX-7GR, depending on the desired beat frequency). The output from M1 at about 25 MHz is lowpass filtered and again amplified. Then the signal is split with a directional coupler (Minicircuits PDC-10-1). The main output is mixed again (with a stable 25MHz source) and serves as the error signal for our PLL. The coupling output on the other hand is amplified up to 10dBm and then sent through a frequency-to-voltage converter (section (B.4.1)). The length of the cable is chosen to be 3 m, such that the output signal crosses zero for 25 MHz input frequency. This signal may be used to frequency-lock the lasers, i.e. to stabilize the frequency of the beat. Due to the fact, that the bandwidth of the PLL is on the order of a few MHz, the beat signal must not deviate from the desired value ($= f_{LO1} + f_{LO2}$) by more than a (few) MHz. In practice, however, the laser frequency may jump by more than that, mainly because of acoustic noise. Thus a frequency lock with a bandwidth of 50 MHz (Fig. B.4) becomes useful. Such a frequency lock can bring the beat frequency back to the desired value and enable relocking of the PLL.

Both, the phase and the frequency error signal are fed into the lockbox, where the gain

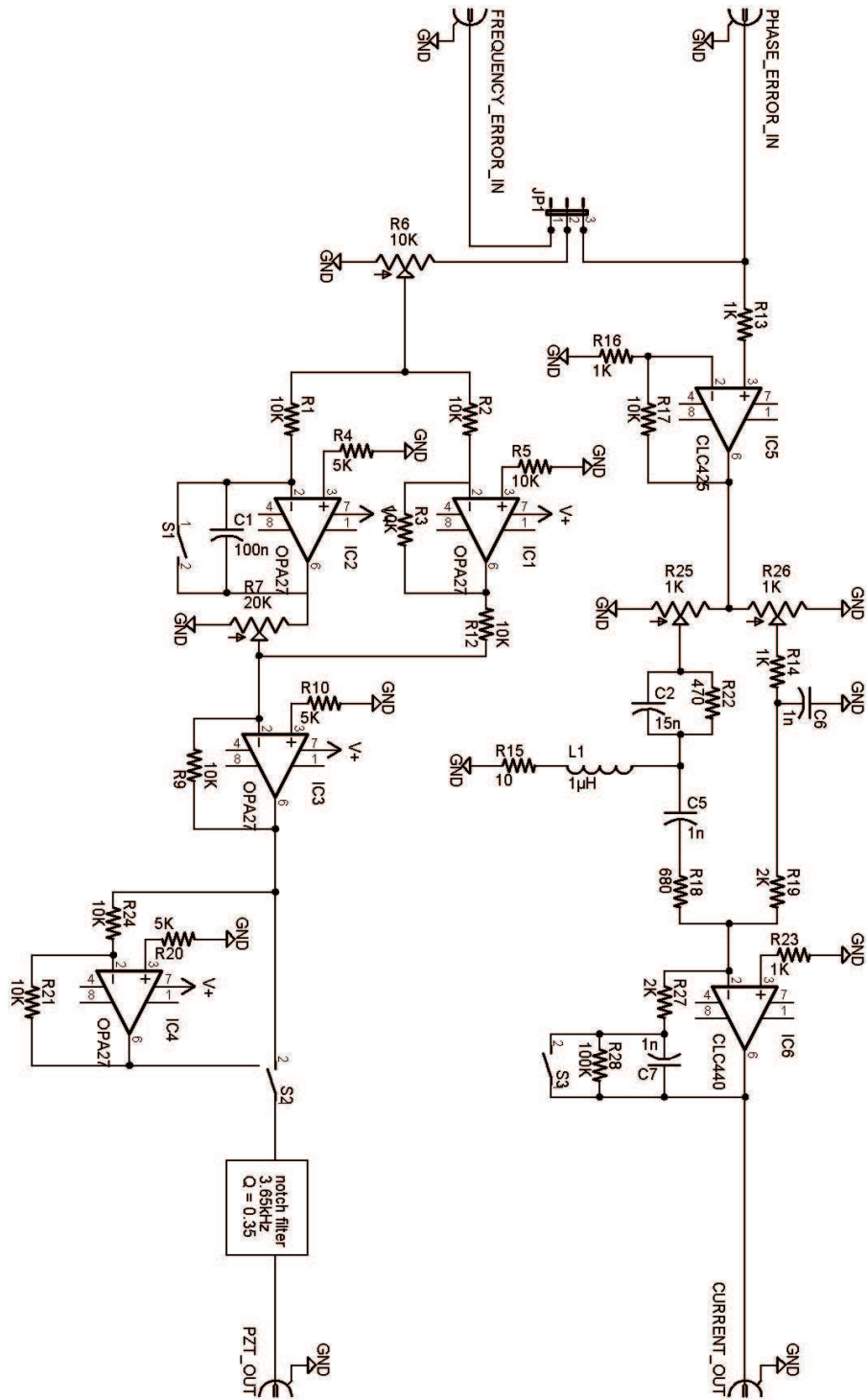


Figure B.8.: Schematic of the servo electronics: As discussed in the following section, the PZT channel may either be used for frequency locking or also for phase locking (Jumper 1).

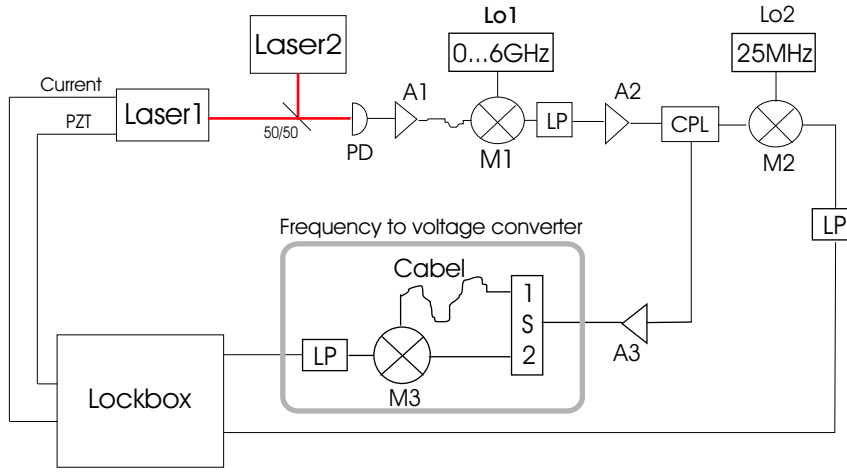


Figure B.9.: Setup for a PLL between two diode lasers

can be adjusted properly. The output of the box is connected to the current driver and the high voltage amplifier for the PZT, respectively.

B.5. Results

B.5.1. The spectrum

In the previous section the spectrum of the beat signal between two independent ECDL was shown. A finite linewidth, due to mechanical noise, was observed. But even in the case, that external noise could have been avoided, the linewidth would have been finite, because of intrinsic random phase fluctuations of the laser. This fundamental limit of the laser linewidth is known as the Schawlow-Townes limit [Sch58] and may be ascribed to spontaneous emission processes.

However, once the phase locked loop is closed, laser 1 is forced to exhibit the same phase fluctuations as laser 2. So the relative phase between laser 1 and 2 stays fixed and the beat between those two is in principle infinitely narrow.

In the actual setup the phase stability is of course not perfect, resulting in a beat signal with a narrow central peak and a broad background (Fig. B.10). The width of the central peak is smaller than the resolution of our spectrum analyzer (100 Hz). For this reason we cannot characterize our PLL by the width of this peak. Instead the ratio of the power in the central peak to the total power is used to quantify the quality of the PLL. For the measurement shown in Fig. B.10 this is

$$\eta := \frac{P_{\text{peak}}}{P_{\text{total}}} \approx 90\%. \quad (\text{B.16})$$

This value for η is reached for basically any beat frequency between 0 and 6 GHz.

In the background of the power spectrum at frequencies of about 1 MHz and 200 kHz from the center two broad peaks are detected. These frequencies of these servo bumps

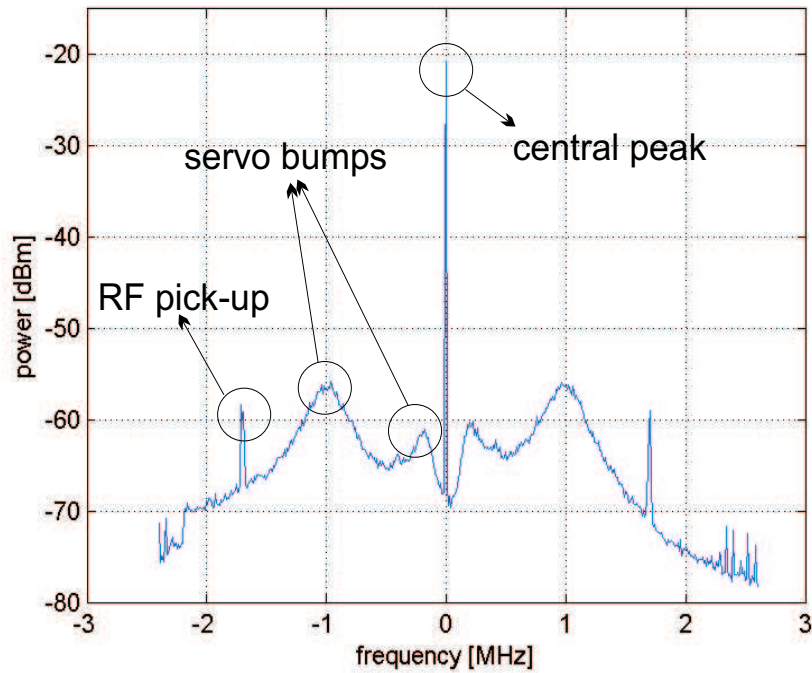


Figure B.10.: Typical beat signal of two phase locked lasers: Below a MHz the noise of the relative phase is suppressed by more than 40 dB. But due to the finite bandwidth of the PLL, the phase noise increases with frequency and reaches maxima (“servo bumps”) at about ± 1 MHz. Beyond the MHz range the signal decreases again, because of the finite laser linewidth (see Fig.B.7).

correspond to the bandwidths of the two channels of our PLL. These values for the bandwidth may be increased a little bit, but not tremendously. The reason is, that feedback beyond a few MHz is very difficult, in particular because modulation of the diode current does not directly translate into a frequency modulation of the laser light any more at such high frequencies.

because many electronic parts as well as the laser diode itself start to respond non-linear at such fast modulations (Fig. B.5).

The other narrow peaks in the background are coming from electronic pick up through the lockbox. They are undesired, however, as long as they are strongly suppressed, they may be neglected.

B.5.2. Phase error

Finally it is shown, how the root-mean-square error of the phase can be derived from the spectrum.

The power spectrum is defined as the square of the Fourier-Transform of the electric

field

$$P(\omega) = \lim_{T \rightarrow \infty} \frac{1}{2T} \left| \int_{-T}^T dt E(t) e^{-i\omega t} \right|^2 \quad (\text{B.17})$$

This may be written as

$$P(\omega) = \lim_{T \rightarrow \infty} \frac{1}{2T} \int_{-T}^T dt \int_{-T}^T dt' E(t)^* E(t') e^{i\omega t} e^{-i\omega t'} \quad (\text{B.18})$$

We introduce $\tau = t' - t$

$$\begin{aligned} P(\omega) &= \lim_{T \rightarrow \infty} \frac{1}{2T} \int_{-T}^T dt \int_{-T}^T d\tau E(t)^* E(\tau + t) e^{-i\omega \tau} \\ &= \int_{-\infty}^{\infty} d\tau R_E(\tau) e^{-i\omega \tau} \end{aligned} \quad (\text{B.19})$$

where

$$R_E(\tau) = \lim_{T \rightarrow \infty} \frac{1}{2T} \int_{-T}^T dt E(t)^* E(\tau + t) \quad (\text{B.20})$$

is the autocorrelation function for the electric field. Thus the power spectrum can be written as the Fourier-Transform of the autocorrelation function of the field.

For a laser or for the beat between two lasers the field is given by

$$E(t) = E_0 e^{i\omega_0 t + i\phi(t)} \quad (\text{B.21})$$

where ϕ is a random but stationary phase; i.e.

$$\begin{aligned} \langle \phi(t) \rangle &= 0 \\ \langle \phi(t)^2 \rangle &=: \Delta \phi_{rms}^2 \end{aligned} \quad (\text{B.22})$$

Plugging (B.21) into (B.20) leads to

$$\begin{aligned} R_E(\tau) &= E_0^2 e^{i\omega_0 \tau} \cdot \lim_{T \rightarrow \infty} \frac{1}{2T} \int_{-T}^T dt e^{i(\phi(t) - \phi(t+\tau))} \\ &= E_0^2 e^{i\omega_0 \tau} \cdot \langle e^{i(\phi(t) - \phi(t+\tau))} \rangle \end{aligned} \quad (\text{B.23})$$

At this point we want to make use of the Gaussian-moment-theorem [Man95], which states

$$\langle e^{i(\phi(t) - \phi(t+\tau))} \rangle = e^{-\frac{1}{2} \langle (\phi(t) - \phi(t+\tau))^2 \rangle} \quad (\text{B.24})$$

Using this theorem, (B.23) writes

$$\begin{aligned} R_E(\tau) &= E_0^2 e^{i\omega_0 \tau} e^{-\frac{1}{2} \langle (\phi(t) - \phi(t+\tau))^2 \rangle} \\ &= E_0^2 e^{i\omega_0 \tau} e^{-\frac{1}{2} [\langle \phi(t)^2 \rangle + \langle \phi(t+\tau)^2 \rangle - 2\langle \phi(t)\phi(t+\tau) \rangle]} \\ &= E_0^2 e^{i\omega_0 \tau} e^{-\Delta \phi_{rms}^2 - \frac{1}{2} R_\phi(\tau)} \end{aligned} \quad (\text{B.25})$$

where $R_\phi(\tau) = \langle \phi(t)\phi(t+\tau) \rangle_t$ is the autocorrelation function of the phase. For a closed PLL we may assume a small phase error ($\phi(t) \ll 1$) and consequently we can approximate (B.25)

$$R_E(\tau) \simeq E_0^2 e^{i\omega_0\tau} \left(1 - \Delta\phi_{rms}^2 - \frac{1}{2}R_\phi(\tau) \right) \quad (\text{B.26})$$

Now we can Fourier-transform $R_E(\tau)$ to get $P(\omega)$

$$\begin{aligned} P(\omega) &= \int_{-\infty}^{\infty} d\tau E_0^2 e^{i(\omega_0-\omega)\tau} (1 - \Delta\phi_{rms}^2 + R_\phi(\tau)) \\ &= E_0^2 \cdot 2\pi \cdot \delta(\omega_0 - \omega) \cdot (1 - \Delta\phi_{rms}^2) + P_\phi(\omega_0 - \omega) \end{aligned} \quad (\text{B.27})$$

with $P_\phi(\omega) = \int_{-\infty}^{\infty} d\tau R_\phi(\tau)e^{-i\omega\tau}$ representing the spectrum of the residual phase fluctuations. Integrating (B.27) over the whole spectrum shows that

$$1 - \Delta\phi_{rms}^2 = \frac{P_{peak}}{P_{total}} = \eta \quad (\text{B.28})$$

That means the root-mean-square of the phase error can easily be estimated, when the relative amount of power in the phase locked peak is known.

Our measured value for η of about 90% therefore leads to

$$\Delta\phi_{rms} \simeq \frac{\pi}{10} \quad (\text{B.29})$$

which is well below a full cycle of 2π .

Bibliography

- [And95] M. H. Anderson, J. R. Ensher, M. R. Matthews, C. E. Wieman und E. A. Cornell, *Science* **269** (1995)
- [Bla04] P. B. Blakie und J. V. Porto, *Phys. Rev. A* **69** (2004)
- [Bug04] C. Buggle, J. Lonard, W. von Klitzing und J. T. M. Walraven, *Phys. Rev. Lett.* **93** (2004)
- [Cho99] D.-I. Choi und Q. Niu, *Phys. Rev. Lett.* **82** (1999)
- [Ciz05] T. Cizmar, V. Garces-Chavez, K. Dholakia und Z. Pemanek, *Appl. Phys. Lett.* **86** (2005)
- [Cri04] M. Cristiani, O. Morsch, N. Malossi, M. Jona-Lasinio, M. Anderlini, E. Courtade und E. A. E, *New. J. Phys.* **12** (2004)
- [CT99] C. Cohen-Tannoudji, B. Diu und F. Laloe, *Quantum mechanics*, vol. 1, W. de Gruyter, 1999, 2nd ed.
- [Dah96] M. B. Dahan, E. Peik, J. Reichel, Y. Castin und C. Salomon, *Phys. Rev. Lett.* **76** (1996)
- [Dav95] K. B. Davis, M. O. Mewes, M. R. Andrews, N. J. van Druten, D. S. Durfee, D. M. Kurn und W. Ketterle, *Phys. Rev. Lett.* **75** (1995)
- [Den02] J. H. Denschlag, J. E. Simsarian, H. Häffner, C. McKenzie, A. Browaeys, D. Cho, K. Helmerson, S. L. Rolston und W. D. Phillips, *J. Phys. B* **35** (2002)
- [Dur87a] J. Durnin, *J. Opt. Soc. Am. B* **4** (1987)
- [Dur87b] J. Durnin, J. J. Miceli und J. H. Eberly, *Phys. Rev. Lett.* **58** (1987)
- [Ess98] T. Esslinger, I. Bloch und T. W. Hänsch, *Phys. Rev. A* **58** (1998)
- [Fal04] L. Fallani, L. D. Sarlo, J. E. Lye, M. Modugno, R. Saers, C. Fort und M. Inguscio, *Phys. Rev. Lett.* **93** (2004)
- [Fol02] R. Folman, P. Krüger, J. Schmiedmayer, J. Denschlag und C. Henkel, *Advances in Atomic, Molecular and Optical Physics* **48** (2002)
- [Gre01] M. Greiner, I. Bloch, T. W. Hänsch und T. Esslinger, *Phys. Rev. A* **63** (2001)

- [Gri00] R. Grimm, M. Weidemüller und Y. B. Ovchinnikov, *Adv. At. Mol. Opt. Phys.* **42** (2000)
- [Gus02] T. L. Gustavson, A. P. Chikkatur, A. E. Leanhardt, A. Gorlitz, S. Gupta, D. E. Pritchard und W. Ketterle, *Phys. Rev. Lett.* **88** (2002)
- [Har91] K. C. Harvey und C. J. Myatt, *Opt. Lett.* **16**, 910 (1991)
- [Hec05] E. Hecht, *Optik*, Oldenbourg Wissenschaftsverlag, 2005, 4th ed.
- [Hor89] P. Horowitz und W. Hill, *The art of electronics*, Cambridge University Press, 1989, 5th ed.
- [Jac02] J. D. Jackson, *Classical Electrodynamics*, Walter de Gruyter, 2002, 3rd ed.
- [Kit87] C. Kittel, *Quantum theory of solids*, New York: Wiley, 1987, 1st ed.
- [Kle89] M. V. Klein und T. E. Furtak, *Optics*, John Wiley and Sons, 1989, 2nd ed.
- [Kuh01] S. Kuhr, W. Alt, D. Schrader, M. Müller, V. Gomer und D. Meschede, *Science* **293** (2001)
- [Lan32] L. Landau, *Phys. Z. Sowjetunion* **2** (1932)
- [Lew02] H. J. Lewandowski, D. M. Harber, D. L. Whitaker und E. A. Cornell, *Phys. Rev. Lett.* **88** (2002)
- [Mac92] K. B. MacAdam, A. Steinbach und C. Wieman, *Am. J. Phys.* **60**, 1098 (1992)
- [Man95] L. Mandel und E. Wolf, *Optical Coherence and Quantum Optics*, Cambridge University Press, 1995
- [Met99] H. J. Metcalf und P. van der Straten, *Laser Cooling and Trapping*, Springer, 1999, 1st ed.
- [Nig97] L. Niggli, T. Lanzl und M. Maier, *J. Opt. Soc. Am. A* **14**, 27 (1997)
- [Pei97] E. Peik, M. B. Dahan, I. Bouchoule, Y. Castin und C. Salomon, *Phys. Rev. A* **55** (1997)
- [Pet02] C. J. Pethik und H. Smith, *Bose-Einstein Condensation in dilute gases*, Cambridge University Press, 2002
- [Rab57] I. I. Rabi, *Phys. Rev.* **51** (1957)
- [S99] J. Söding, D. Guéry-Odelin, P. Desbiolles, F. Chevy, H. Inamori und J. Dalibard, *Appl. Phys. B* **69** (1999)
- [Sch58] A. L. Schawlow und C. H. Townes, *Phys. Rev.* **112** (1958)
- [Sch68] L. Schiff, *Quantum mechanics*, New York: McGraw Hill, 1968, 3rd ed.

- [The05] M. Theis, *Optical Feshbach Resonances in a Bose-Einstein Condensate*, PhD thesis, Universität Innsbruck (2005)
- [Tho04] N. R. Thomas, N. Kjrgaard, P. S. Julienne und A. C. Wilson, Phys. Rev. Lett. **93** (2004)
- [Vas90] A. Vasara, J. Turunen und A. T. Friberg, J. Opt. Soc. Am. A **6**, 1748 (1990)
- [Was93] C. Waschke, H. Roskos, R. Schwedler, K. Leo, H. Kurz und K. Köhler, Phys. Rev. Lett. **70** (1993)
- [Wu03] B. Wu und Q. Niu, New. J. Phys. **5** (2003)
- [Zen32] G. Zener, Proc. R. Soc. London, Ser. A **137** (1932)